Grainenergy release governs mobility of debris flow due to solid–liquid mass release

Grain-energy release governs mobility of debris flow due to solid-liquid mass release

Zhixian Cao [1*], Ji Li[1, 2], Alistair Borthwick[3], Qingquan Liu[4**], Gareth Pender[5]

[1] State Key Laboratory of Water Resources and Hydropower Engineering Science, Wuhan University, Wuhan, China;

[2] Zienkiewicz Centre for Computational Engineering, College of Engineering, Swansea University, Swansea, UK;

[3] Institute for Infrastructure and Environment, The University of Edinburgh, Edinburgh, UK;

[4] Department of Mechanics, Beijing Institute of Technology, Beijing, China;

[5] Institute for Infrastructure and Environment, Heriot-Watt University, Edinburgh, UK.

Correspondence

Zhixian Cao, State Key Laboratory of Water Resources and Hydropower Engineering Science, Wuhan University, Wuhan 430072, China.

Email: zxcao@whu.edu.cn

Qingquan Liu, Department of Mechanics, Beijing Institute of Technology, Beijing, 100081, China

Email: liuqq@bit.edu.cn

ABSTRACT

Debris flows often exhibit high mobility, leading to extensive hazards far from their sources. Although it is known that debris flow mobility increases with initial volume, the underlying mechanism remains uncertain. Here, we reconstruct the mobility-volume relation for debris flows using a recent depth-averaged two-phase flow model without evoking reduced friction coefficient, challenging currently prevailing friction-reduction hypotheses. Physical experimental debris flows driven by solid-liquid mass release and extended numerical cases at both laboratory and field scales are resolved by the model. For the first time, we probe into the energetics of the debris flows and find that, whilst the energy balance holds and fine and coarse grains play distinct roles in debris flow energetics, the grains as a whole release energy to the liquid due to inter-phase and inter-grain size interactions, and this grain-energy release correlates closely with mobility. Despite uncertainty arising from the model closures, our results provide insight into the fundamental mechanisms operating in debris flows. We propose that debris flow mobility is governed by grain-energy release, thereby facilitating a bridge between mobility and internal energy transfer. Initial volume of debris flow is inadequate for characterizing debris flow mobility, and a friction-reduction mechanism is not a prerequisite for the high mobility of debris flows. By contrast, inter-phase and inter-grain size interactions play primary roles and should be incorporated explicitly in debris flow models. Our findings are qualitatively encouraging and physically meaningful, providing implications not only for assessing future debris flow hazards and informing mitigation and adaptation strategies, but also for unravelling a spectrum of earth surface processes including heavily sediment-laden floods, subaqueous debris flows and turbidity currents in rivers, reservoirs, estuaries and ocean.

KEYWORDS: debris flows; solid-liquid mass release; high mobility; mobility-volume relation; energy transfer; grain-energy release

1 INTRODUCTION

Debris flows form when masses of poorly sorted sediments, agitated and saturated by water, surge down steep slopes in response to gravitational effects, and can grow dramatically in speed and size by entraining materials from beds and banks (Iverson, 1997). The severity of these hazards is largely dependent on the speed and travel distance, which are collectively described as “mobility” (Iverson et al., 2015). Owing to their destructive power, debris flows can produce significant natural hazards. Often, debris flows generated by solid-liquid mass releases exhibit exceptionally high mobility leading to catastrophic disasters extending far beyond the source zone (Iverson, 1997; Legros, 2002; Rickenmann, 2005; Lucas, Mangeney, & Ampuero, 2014; Gregoretti, Degetto, Bernard, & Boreggio, 2018; Chen, Liu, Wang, Zao, & Zhou, 2019). Field observations and experimental measurements indicate that debris flow mobility increases with initial volume (Iverson, 1997; Rickenmann, 2005), and is further enhanced by bed erosion, water content, and grain-size heterogeneity (Iverson, 1997; Legros, 2002; Rickenmann, 2005). Several empirical relationships have been proposed to estimate debris flow mobility on the basis of initial volume alone (e.g., Corominas, 1996; Rickmann, 1999, 2005). Field data also reveal that for a given volume, debris flows, as typical liquid-solid two-phase flows, exhibit much higher efficiency than avalanches and rock falls (Hayashi & Self, 1992; Iverson, 1997; Vallance & Scott, 1997; Legros, 2002), which behave physically as single-phase granular flows. Usually, the mobility of debris flow is characterized by the horizontal run-out distance L or efficiency e (= L/H where H is the vertical fall height) (Iverson, 1997; Legros, 2002; Lucas et al., 2014; Rickenmann, 2005). In particular, for extremely large volume events, the efficiency of non-channelized natural debris flow

can reach up to 25 (Iverson, 1997). Debris flows can also be generated by run-off (e.g., Kean, McCoy, Tucker, Staley, & Coe, 2013; Hürlimann, Abanco, Moya, & Vilajosana, 2014; Ma, Deng, & Wang, 2018), in which case mobility is mainly controlled by the triggering discharge (Lanzoni, Gregoretti, & Stancanelli, 2017). The present study focuses on debris flow due to solid-liquid mass release.

However, the mechanisms underlying the high mobility of debris flows due to solid-liquid mass release remain poorly understood (Iverson, 1997; Lucas et al., 2014). Many fundamentally distinct friction-reduction hypotheses have been proposed to explain the high mobility of general geophysical mass flows (e.g., avalanches, rock falls and debris flows), including those based on velocity-dependent friction weakening (Lucas et al., 2014), fluidization by water (Legros, 2002; Pudasaini & Miller, 2013), entrainment (Hungr & Evans, 2004; Mangeney, Tsimring, Volfson, Aranson, & Bouchut, 2007; Lube et al., 2012), pore fluid pressure (Iverson et al., 2011; Iverson et al., 2015), grain-size distribution (de Haas, Braat, Leuven, Lokhorst, & Kleinhans, 2015; Kaitna, Palucis, Yohannes, Hill, & Dietrich, 2016), grain segregation-induced momentum advection (Johnson et al., 2012) or friction decrease (Linares-Guerrero, Goujon, & Zenit, 2007), flash friction heating (Goren & Aharonov, 2007; Singer, McKinnon, Schenk, & Moore, 2012; Wang, Dong, & Cheng, 2017), dynamic fragmentation (Perinotto et al., 2015), acoustic fluidization (Johnson et al., 2016), and an air cushion trapped underneath a moving mass (Shreve, 1968). Although certain mechanisms may be appropriate for particular site-specific events, none of these hypotheses provides a universal explanation for the high mobility of debris flows (Lucas et al., 2014; Iverson, 2016), which essentially incorporate diverse complicated physical processes (Lucas et al., 2014), including inter-phase interactions between water and sediments, multiple grain sizes, and substantial mass

exchange with the bed. Furthermore, the relation between mobility and initial volume cannot be properly reconstructed without using reduced friction coefficients (Lucas et al., 2014; Johnson et al., 2016) with much lower values than generally accepted for geological materials (Singer et al., 2012). Actually, most friction-reduction hypotheses are necessarily rooted in conjecture rather than fact (Iverson, 2016) because hardly any experimental evidence is available for validation purposes (Utili, Zhao, & Houlsby, 2015; Iverson, 2016). Also, none of these hypotheses is able to fully resolve debris flow dynamics because of the underlying assumptions concerning single-phase dry granular flow without water (Shreve, 1968; Hungr and Evans, 2004; Linares-Guerrero et al., 2007; Mangeney et al., 2007; Lucas et al., 2014; Johnson et al., 2016), single (uniform) grain size (Shreve, 1968; Hungr & Evans, 2004; Mangeney et al., 2007; Goren et al., 2007; Lucas et al., 2014; Johnson et al., 2016), and negligible mass exchange with the bed (Shreve, 1968; Goren et al., 2007; Lucas et al., 2014; Johnson et al., 2016).

Computational modelling holds great promise for resolving the mechanisms behind the high mobility of debris flows. The past several decades have witnessed the development and application of many numerical models of debris flows, the majority being based on depth-averaged single-phase flow formulations (e.g., Takahashi, Nakagawa, Harada, & Yamashiki, 1992; Iverson, 1997; McDougall & Hungr, 2005; Medina, Hürlimann, & Bateman, 2008; Armanini, 2009; Rosatti & Begnudelli, 2013; Iverson & George, 2014; Lucas et al., 2014; Frank, McArdell, Huggel, & Vieli, 2015; Cuomo, Pastor, Capobianco, & Cascini, 2016; Xia, Li, Cao, Liu, & Hu, 2018; Federico & Cesali, 2019; Gregoretti et al., 2019). Notably, a single-phase flow model based on energy conservation was proposed by Wang, Morgenstern, & Chan (2010). In general however, only the velocity of water-sediment mixture is solved in these

models, and the relative motions and interactions between the water and sediment phases are not explicitly incorporated, even though both are primary features of debris flows (e.g., Iverson, 1997; Pudasaini, 2012). In this connection, two-phase flow theory is certainly the way forward (Armanini, 2013), whereby water and sediment phases are separately resolved according to their respective mass and momentum conservation laws. Indeed, depth-averaged two-phase flow models are not new in debris flow modelling (e.g., Pitman & Le, 2005; Pelanti, Bouchut, & Mangeney, 2008; Pailha & Pouliquen, 2009; Pudasaini, 2012; Kowalski & McElwaine, 2013; Bouchut, Fernandez-Nieto, Mangeney, & Narbona-Reina, 2015). However, previous two-phase flow models have suffered from several major shortcomings. First, they are confined to single-sized sediment transport. In practice, sediments in debris flows may be heterogeneous with widely distributed sizes, ranging from clay (particle diameter $\approx 10^{-5}$ m) to boulders (particle diameter $\approx 10^{1}$ m) (Iverson, 1997). Grain size data reveal the oversimplification of debris flow models that presume the sediment mixture comprises particles of a single grain size, and they also reinforce the notion that multiple grain sizes may be critical to debris flow dynamics (Iverson, 1997). Second, existing depth-averaged two-phase flow models have exclusively ignored mass exchange between the flow and the bed, a vital physical aspect of debris flows. Inevitably, they are restricted to modeling debris flows over fixed beds. Third, existing two-phase flow models have generally neglected the effects of liquid and solid fluctuations. Notably, inclusion of stresses due to liquid and solid fluctuations has been demonstrated to be important in reproducing debris flow kinetics (Li, Cao, Hu, Pender, & Liu, 2018b).

Here, we apply a recently developed numerical depth-averaged two-phase flow model (Li, Cao, Hu, Pender, & Liu, 2018a) to reproduce the full sets of USGS

151 experimental debris flows reported by Iverson et al. (2011) and then resolve a
152 spectrum of laboratory- and field-scale numerical cases designed according to the
153 USGS experiments. Unlike previous numerical models based on reduced friction
154 coefficients (Lucas et al., 2014), the friction coefficients used here have values within
155 the conventional ranges. We then probe into the energetics of debris flows by
156 evaluating the energy components and energy changes of both the liquid and solid
157 phases for all the aforementioned experimental and numerical cases. Energy transfer
158 within debris flow is linked with its mobility. This, the first work of its kind, is certainly
159 warranted given that debris flow mobility has perplexed scientists for decades.

160 The present work aims to enhance the understanding of debris flow mobility based on
161 numerical solutions from a two-phase flow model (Li et al., 2018a). The model has
162 incorporated as much physics as possible to expand capability and minimize
163 uncertainty, and has been validated against all available observed data from USGS
164 experiments (Iverson, Logan, LaHusen, & Berti, 2010; Iverson et al., 2011). In
165 particular, it features a physical step forward in debris flow modelling by incorporating
166 inter-phase and inter-grain size interactions, multiple grain sizes, mass exchange with
167 the bed and strong liquid and solid fluctuations. Yet, like other numerical models for
168 general earth surface flows, a set of relationships has to be introduced to close the
169 model, and quantitatively some degree of uncertainty is inevitable. In particular, the
170 closure models for inter-grain size interaction, liquid and solid fluctuations, and mass
171 exchange with the bed are tentatively employed for modelling debris flow, given that
172 no generally valid closure models have been forthcoming to date. Although the
173 closure models remain imperfect, the modelling results provide some insight into the
174 fundamental mechanisms operating in debris flows.

175

176 ## 2 METHODS

177 ### 2.1 Case descriptions

178 #### 2.1.1 USGS debris flow experiments

179 A series of laboratory-scale experiments was conducted at the USGS debris-flow
180 flume (Iverson, 1997; Iverson et al., 2011). The experiments involved unsteady,
181 non-uniform debris flows from initiation to deposition. The USGS debris-flow flume
182 comprised a straight rectangular concrete channel, 95 m long, 2 m wide, and 1.2 m
183 deep (Figure 1), connected to an adjacent runout pad. A 2 m high vertical headgate
184 was used to retain static debris prior to its release. For $0 \leq x \leq$ 74 m, the flume bed
185 had uniform slope, $\theta =$ 31º, whereas for $x >$ 74 m, the bed slope tended towards
186 horizontal. Approximately 6 m^3 of a water-saturated sediment mixture called SGM, of
187 porosity $p =$ 0.49 (corresponding to water content $\theta_f = p =$ 0.49), and composed of
188 about 53% gravel, 37% sand, and 7% mud-sized grains with standard deviation $\sigma =$
189 8.87, was released abruptly from a headgate and propagated downslope. Table S1
190 lists the detailed sediment composition of SGM. Here two typical experimental cases
191 are revisited. For the erodible-bed experiment (labelled “EXP-E”), bed sediment of
192 unsaturated SGM with water content $\theta_f =$ 0.28, volume 10.9 m^3, thickness ~12 cm
193 initially covered the uniformly sloping ramp from $x =$ 6 m to 53 m. For the fixed-bed
194 experiment (labelled “EXP-F”), the debris flow was released in the absence of bed
195 sediment. Table S2 in Supporting Information lists details of the experimental cases.

196

197

198 **FIGURE 1** Flume geometry for USGS debris flow experiments [from Iverson et al.
199 (2011)].

200

201 **2.1.2 Laboratory-scale numerical cases**

202 Using numerical simulation, we extend the parameter ranges covered in the USGS
203 experiments to investigate the influence of initial debris flow volume. Also, the effects
204 of bed erosion, water content, and grain-size heterogeneity are investigated (Table
205 S3). Furthermore, a similar channel with the same length L_0 as that used in USGS
206 experiments but different sloping angle ($\theta =$ 40º) is used (Figure 2a). We classify the
207 case studies into fixed-bed and erodible-bed studies; therefore, laboratory-scale
208 numerical cases are labelled “FBS” and “EBS”. Briefly, the initial volume of the
209 released debris flow, which is composed of a water-saturated sediment mixture SGM,
210 ranges from 1 m^3 to 1600 m^3 in order to investigate the volume effect. Then, for each
211 debris flow (volume varying from 6 m^3 to 1600 m^3), the bed sediment, which is the
212 same as that used in USGS experiment, is placed on the sloping ramp to study the
213 effect of bed erosion (i.e., EBS cases). To investigate the effect of water content, the
214 initial water content θ_f of the released debris flow is reduced from 0.49 to 0.3 or 0.1,
215 and to address the effect of heterogeneity, the grain-size heterogeneity is adjusted by
216 altering the standard deviation of sediment composition (i.e., σ was set to 13.17 or
217 4.25), while retaining the same median size d_{50} (= 3.22 mm, the particle size at which

50% of the sediments are finer). Except for the initial values of flow thickness, water content and sediment composition of the released debris flow, and bed elevation (see Table S3 in Supporting Information), all other parameters are kept the same as in the experiments.

2.1.3 Field-scale numerical cases

The field-scale numerical case studies are qualitatively similar to the laboratory-scale cases described above. The computational domain has an upstream ramp of uniform inclination angle of $\theta =$ 31º or 40º, length L_0 and height H_0, which joins (at its downstream end) a horizontal runout pad (Figure 2b). For intermediate field-scale cases (labelled “FBM” and “EBM”), the length L_0 and width B of the sloping channel are respectively 400 m and 20 m, whereas for large field-scale cases (labelled “FBL” and “EBL”), the corresponding length L_0 and width B are 1600 m and 50 m, respectively. First, the effect of initial debris flow volume is investigated. For the intermediate field-scale cases, the initial volume of debris flow ranges from 30 m^3 to 1.2 × 10^7 m^3, whereas for the large field-scale cases, the initial volume varies from 1000 m^3 to 10^9 m^3. The released debris flow is composed of a water-saturated sediment mixture SGM (i.e., $\theta_f =$ 0.49 and $\sigma =$ 8.87), which is the same as in the USGS experiments. Then the effects of bed erosion, water content, and grain-size heterogeneity are studied. In particular, to investigate the effect of bed erosion, for EBM cases, the unsaturated bed sediment SGM ($\theta_f =$ 0.28) of volume $V_b =$ 1500 m^3 covers the sloping ramp, whereas for EBL cases, that of volume $V_b =$ 10^5 m^3 is placed on the sloping ramp. To address the respective effects of water content and

grain-size heterogeneity, for both FBM and FBL cases, we consider reduced water content (i.e., $\theta_f =$ 0.3 or 0.1) and adjusted sediment composition (i.e., $\sigma =$ 13.17 or 4.25 with $d_{50} =$ 3.22 mm) of the released debris flow, following the FBS cases. Details are summarized in Tables S4 and S5 in Supporting Information.

FIGURE 2 Flume geometry used in (a) laboratory-scale numerical case studies (adapted from Iverson et al., 2011); (b) field-scale numerical case studies. The topography has an upstream ramp of uniform inclination angle θ, length L_0 and height H_0, followed by a horizontal runout pad at the downstream end.

2.2 Modelling methods

A depth-averaged two-phase flow model (Li et al., 2018a) is used to resolve the spatial and temporal evolution of debris flow, from initiation to final stoppage. The model is based on a previous fixed-bed model (Li, et al., 2018b), extended to erodible bed flows. On the basis of the numerical solutions, debris flow mobility and energy components can be readily determined. The present model is constructed according to continuum mechanics principles, in which inter-phase interaction is explicitly taken into account, unlike single-phase flow models (e.g., Takahashi et al., 1992; Iverson, 1997; McDougall & Hungr, 2005; Medina et al., 2008; Armanini, 2009; Rosatti & Begnudelli, 2013; Iverson & George, 2014; Lucas et al., 2014; Frank et al., 2015; Cuomo et al., 2016; Xia et al., 2018; Federico & Cesali, 2019; Gregoretti et al., 2019).

Unlike existing two-phase flow models (Pitman & Le, 2005; Pelanti et al., 2008; Pailha & Pouliquen, 2009; Pudasaini, 2012; Kowalski & McElwaine, 2013; Bouchut et al., 2015), the present model incorporates multiple grain sizes (noting the typically broad distribution of grain size, which directly affects debris flow mobility (Johnson et al., 2012; de Haas et al., 2015; Kaitna et al., 2016)), mass exchange with the bed (that may affect mobility (Iverson, 1997; Hungr & Evans, 2004; Mangeney et al., 2007; Iverson et al., 2011; Lube et al., 2012)), and stresses due to strong liquid and solid fluctuations. The present model along with the governing equations are briefly described in Text S1 in Supporting Information.

A set of relationships is introduced to close the model, as is common with all such models in earth science. Although all the closure relations used in the two-phase flow model of Li et al. (2018a) were previously established for shallow water hydro-sediment-morphodynamics, some of them are also tentatively applied in debris flow modelling, and are inevitably empirical to some extent. We use the Coulomb friction law and Manning's equation to determine the bed shear stresses for solid and liquid phases respectively (Iverson, 1997; Pudasaini, 2012; Iverson & George, 2014). In practice, the Coulomb friction law is usually applied to friction-dominated debris flows. When debris flows are composed of coarse grains, they are mainly affected by a collisional, or a coupled frictional and collisional, regime (Lanzoni et al., 2017), for which a constitutive equation accounting for both the frictional and collisional stresses is warranted. Inter-phase interaction is modelled by means of the Gidaspow drag correlation (Gidaspow, 1994), which combines the Ergun equation for dense

285 water-sediment mixtures and a power law for dilute suspensions. Inter-grain size
286 interaction is based on linear velocity-dependent drag, grain-grain surface interaction,
287 and remixing force components (Gray & Chugunov, 2006). To date, there have been
288 hardly any studies on inter-grain size interaction in debris flows. Thus, a closure
289 relationship derived for a simple binary mixture (Gray & Chugunov, 2006) is
290 tentatively used for debris flows (which are nevertheless composed of more broadly
291 distributed grain sizes). Debris flows are characterized by strong fluctuations in liquid
292 and solid motions (Iverson et al., 1997). However, generally valid closure models
293 remain unavailable. By analogy to turbulent motion, the stress arising from liquid
294 fluctuation is approximated by a conventional turbulent kinetic energy – dissipation
295 rate ($k-\varepsilon$) model (Rodi, 1993) originally developed for the flow of pure fluid without
296 sediment. The stress due to solid fluctuation is determined by a first-order model
297 based on the kinetic theory of granular flows under dilute flow conditions (Jenkins &
298 Richman, 1985). Wu's formula (Wu, 2007) is used to estimate the sediment transport
299 rate of each size fraction. An active layer formulation (Hirano, 1971) represents
300 stratigraphic evolution of the bed. A plethora of closure relations has been proposed
301 to estimate mass exchange with the bed induced by geophysical mass flows (see e.g.
302 Pitman et al., 2003; McDougall & Hungr, 2005; Medina et al., 2008; Iverson, 2012;
303 Pirulli & Pastor, 2012). Unfortunately, these relations suffer from shortcomings
304 because understanding of the underlying physical processes remains far from clear
305 (as discussed by e.g. Hungr & Evans, 2004; Iverson, 2012). Critically, most relations
306 do not consider the effect of particle size, which is questionable from a physical

307 perspective because fine grains are easier to erode than large blocks (Pirulli & Pastor,
308 2012). Given the fact that no generally valid mass exchange relations are available
309 for erodible-bed debris flows, Li et al. (2018a) tentatively employed the closure model
310 widely used in fluvial hydraulics to estimate mass exchange between the debris flow
311 and the bed. This closure model has previously been found to perform significantly
312 better than an alternative analytical relation (Medina et al., 2008).

313 The governing equations are numerically solved using an adapted version of a
314 well-balanced numerical algorithm (Cao, P. Hu, K. Hu, Pender, & Liu, 2015a). The
315 computational domain consists of a uniformly sloping ramp and adjacent
316 (channelized) horizontal runout pad of unlimited length (Figures 1 and 2). For USGS
317 debris flow experiments and laboratory-scale numerical cases, the spatial step $\Delta x =$
318 0.1 m, whereas for field-scale numerical cases, $\Delta x =$ 0.4 m. Numerical simulation is
319 performed until the debris flow stops, at which time the run-out distance is evaluated.
320 Initial values of flow thickness, volumetric sediment concentration, and bed elevation
321 are case specific (see Tables S3-S5 in Supporting Information). The initial velocity,
322 fluctuation kinetic energy, and dissipation rate are set to zero. Both the upstream and
323 downstream boundary conditions are prescribed constant because the channel is
324 sufficiently long to ensure that forward and backward waves of the debris flow do not
325 reach either end boundary during the simulation.

326 Li et al. (2018a) provide a detailed description of the depth-averaged two-phase flow
327 model equations along with model closure and the numerical algorithm. The model
328 incorporates the leading-order physical factors in the mass and momentum

329 conservation equations, such as gravitation, resistance, inter-phase and inter-grain
330 size interactions. Importantly, for the first time, this model performs well when tested
331 against the full sets of USGS experimental debris flows over fixed-beds (Li et al.,
332 2018b) and erodible-beds (Li et al., 2018a), and is able to resolve fundamental
333 mechanisms in debris flows (e.g., significant effects of multiple grain sizes, bed
334 erosion and initial water content) that have been found by observed field data
335 (Iverson, 1997). It is nevertheless appreciated that more delicate and refined
336 mechanisms may exist in debris flows, which, if incorporated, could modify the
337 modelling results (e.g., collisional solid stress (Lanzoni et al., 2017) and
338 non-Newtonian liquid viscous stress (Pudasaini, 2012)). However, these are most
339 likely to be second- and higher-order factors; it is our intention to incorporate these in
340 a future version of the model.
341 Note that compared with the friction coefficient values previously used (Li et al.,
342 2018a), the values adopted in the present study have been slightly adjusted within
343 the conventional range to reduce the residual bulk energy of debris flow to a minimum,
344 while ensuring the computed kinetic variables (e.g., velocity, thickness, bed
345 deformation, sediment concentration) match measured data (Iverson et al., 2011).
346 Briefly, the Manning roughness has been tuned by 5.7%, increasing from 0.028 to
347 0.0296 $s.m^{-1/3}$, and the solid friction coefficient has been tuned by 7.7%, reducing
348 from 0.839 to 0.774. In relation to Cases EXP-F and EXP-E, Figures S1 and S2 show
349 time series of front locations and flow surface elevations above the bed predicted by
350 the present two-phase flow equation (TPE) model using previous (Li et al., 2018a)
351 and adjusted friction coefficients, along with measured data (Iverson et al., 2011). For

Case EXP-E, Figure S3 compares the measured bed elevation time histories with predictions by the TPE model, utilizing previous values of friction coefficient (Li et al., 2018a) and adjusted friction coefficients. As can be seen from Figures S1-S3, the computed results by the TPE model with adjusted friction coefficients agree rather well with measured data and predictions by TPE model with previous friction coefficients (Li et al., 2018a).

2.3 Energy calculation

We calculate the energy components from initiation to stoppage based on physical variables (e.g. bed elevation, flow depth, flow velocity, volumetric concentration, fluctuation kinetic energy, and dissipation rates of the liquid and solid phases) resolved using the depth-averaged two-phase flow model (Li et al., 2018a) described above. Kinetic energy (E_K), fluctuation kinetic energy (E_{TK}), gravitational potential energy (E_G), and potential energy due to sediment exchange with the bed (E_{Gb}) are evaluated by trapezoidal integration of local variables over space at a specific time. Energy dissipation due to bed resistance (E_R) and fluctuation motions (E_D) and the work done by inter-phase (E_{fs}) and inter-grain size interaction forces (E_{ss}) are calculated by integrating variables in both space and time, again using the trapezoidal rule. Details of the energy calculation methods are described as follows.

2.3.1 Gravitational potential energy

The gravitational potential energy of the solid phase in a debris flow system, E_{Gs}, at any time t is

$$E_{Gs}(t) = \int [\sum_{k=1}^{N} \rho_s h_i C_{ki} g H_i B_i] \Delta x \quad (1)$$

where Δx is the length of the control volume (Figure 3); subscript i denotes the control volume index; subscript k denotes the k-th sediment size within N size classes; subscript s represents the solid phase; g is gravitational acceleration; h_i is debris flow depth of the i-th control volume; C_{ki} is depth-averaged size-specific volumetric sediment concentration of the i-th control volume; ρ_s is density of the solid phase; B_i is width of the i-th control volume; H_i is vertical distance between the mass center of debris flow of the i-th control volume and the datum level (Figure 3) set at the horizontal elevation of the run-out pad. H_i is calculated from

$$H_i = (h_i/2 + z_{bi}(t))\cos\theta + (x_d - x_i)\sin\theta \quad (2)$$

where x_d is distance from the mass release point along the channel to the point where the flow reaches the horizontal reference datum; θ is the bed slope angle.

The gravitational potential energy of the liquid phase in the debris flow system, E_{Gf}, at any time t is

$$E_{Gf}(t) = \int [\rho_f h_i C_{fi} g H_i B_i] \Delta x \quad (3)$$

where subscript f represents the liquid phase; and C_{fi} is the depth-averaged volume fraction of the liquid phase of the i-th control volume.

FIGURE 3 Sketch of control volume used for energy calculation. H_i is vertical distance between the mass center of debris flow of the i-th control volume and the datum level, and is accordingly defined by Eq. (2).

397

398 **2.3.2 Kinetic energy**

399 The kinetic energy of the solid phase of the debris flow system, E_{Ks}, is calculated as

400 $$E_{Ks}(t) = \int [\sum_{k=1}^{N} (\frac{1}{2} \rho_s h_i C_{ki} U_{ski}^2 B_i)] \Delta x \quad (4)$$

401 where U_{ski} is the size-specific depth-averaged velocity of the solid phase in the $x-$
402 direction of the $i-$th control volume. Likewise, the kinetic energy of the liquid phase
403 of the debris flow system, E_{Kf}, at any time is defined as

404 $$E_{Kf}(t) = \int [\frac{1}{2} \rho_f h_i C_{fi} U_{fi}^2 B_i] \Delta x \quad (5)$$

405 where U_{fi} is the depth-averaged velocity of liquid phase in the $x-$direction of the
406 $i-$th control volume.

407

408 **2.3.3 Fluctuation kinetic energy**

409 Kinetic energy due to fluctuations of solid motions in the debris flow system is
410 calculated by

411 $$E_{TKs}(t) = \int [\sum_{k=1}^{N} (\rho_s h_i C_{ki} TK_{ski} B_i)] \Delta x \quad (6)$$

412 where TK_{ski} is the size-specific depth-averaged fluctuation kinetic energy of the solid
413 phase of the $i-$th control volume. The fluctuation kinetic energy of the liquid phase in
414 the debris flow system is determined by

$$E_{TKf}(t) = \int [\rho_f h_i C_{fi} TK_{fi} B_i] \Delta x \tag{7}$$

where TK_{fi} is the depth-averaged fluctuation kinetic energy of the liquid phase of the $i-$th control volume.

2.3.4 Potential energy due to sediment exchange with the bed

In general, two distinct mechanisms are involved in sediment exchange with the bed: sediment entrainment due to inter-phase and inter-grain size interactions; and sediment deposition resulting primarily from gravitational action. Physically, eroded bed sediments can increase the potential energy of debris flow which may be converted into kinetic energy downslope, and *vice versa*. Similar to the calculation of the potential energy of debris flow, the potential energy due to sediment exchange with the bed is

$$E_{Gb}(t) = \int [\rho_0 h_{bi} g H_{bi} B_i] \Delta x \tag{8}$$

where subscript b refers to bed material; $\rho_0 = \rho_f \theta_f + \rho_s (1-p)$ is the bed density, p is bed sediment porosity, θ_f is water content of the bed (normally $\theta_f \le p$), $h_{bi} = z_{bi}(t=0) - z_{bi}(t)$ is bed deformation depth; and z_{bi} is bed elevation of the $i-$th control volume. H_{bi} is the vertical distance between the mass center of the $i-$th control volume for bed deformation and the datum level, and is accordingly defined as follows (Figure S4)

$$H_{bi} = (h_{bi}/2 + z_{bi}(t))\cos\theta + (x_d - x_i)\sin\theta \tag{9}$$

436 **2.3.5 Energy dissipation due to bed resistance and fluctuation motions**

437 During a time interval Δt, the liquid phase and size-specific solid phase travel
438 distances $U_{fi}\Delta t$ and $U_{ski}\Delta t$ over the bed, and so the energy loss due to bed
439 resistance in a unit volume during a time interval is defined as

440 $$E_{Ri,\Delta t} = \tau_{fbi} U_{fi} B_i \Delta x \Delta t + \sum_{k=1}^{N} \tau_{s_k bi} U_{ski} B_i \Delta x \Delta t \tag{10}$$

441 where τ_{fbi} and $\tau_{s_k bi}$ are bed shear stresses for the liquid and size-specific solid
442 phases of the $i-$ th control volume. Therefore, the time-dependent energy loss of
443 the debris flow system, induced by bed resistance, is

444 $$E_R(t) = \iint [\tau_{fbi} U_{fi} B_i + \sum_{k=1}^{N} \tau_{s_k bi} U_{ski} B_i] \Delta x \Delta t \tag{11}$$

445 Likewise, the energy dissipation due to fluctuations is

446 $$E_D(t) = \iint [\rho_f h_i C_{fi} \varepsilon_{fi} B_i + \sum_{k=1}^{N} \rho_s h_i C_{ski} \varepsilon_{ski} B_i] \Delta x \Delta t \tag{12}$$

447 where ε_{fi} and ε_{ski} are depth-averaged dissipation rates for the liquid and solid
448 phases, respectively.

449

450 **2.3.6 Work done by inter-phase and inter-grain size interactions**

451 The work done by the interaction force can be computed in a similar way to the
452 energy loss induced by bed resistance. For size-specific solid grains, the interaction
453 forces of the $i-$th control volume include a size-specific depth-averaged interphase
454 interaction force component $F_{fs_k i}$ for the solid phase and a size-specific

depth-averaged inter-grain size interaction force component $F_{s-s_k i}$, exerted on the $k-$th solid phase by the other solid-phase constituents, and which satisfies $\sum(F_{s-s_k i})=$ 0. Thus for the solid phase of the debris flow system, the work done by the inter-phase interaction force is

$$E_{fs} = \iint [\sum_{k=1}^{N} F_{fs_k i} U_{ski} B_i] \Delta x \Delta t \tag{13}$$

and the work done by the inter-grain size interaction force is

$$E_{ss} = \iint [\sum_{k=1}^{N} F_{s-s_k i} U_{ski} B_i] \Delta x \Delta t \tag{14}$$

For the liquid phase, the interaction force of the $i-$th control volume consists of the sum of interphase interaction forces, $\sum F_{s_k fi}$. Accordingly, the work done by the interphase interaction force is

$$E_{sf} = \iint [\sum_{k=1}^{N} F_{s_k fi} U_{fi} B_i] \Delta x \Delta t \tag{15}$$

2.3.7 Energy change

The energy change in the debris flow relative to initial conditions is defined as

$$\Delta E = E_G + E_K + E_{TK} + E_R + E_D - E_{T0} - E_{Gb} \tag{16}$$

where E_{T0} denotes the initial energy of debris flow. Energy changes of the solid phase, ΔE_s, the liquid phase, ΔE_f, and the size-specific grains ΔE_{sk} are similarly defined.

3 RESULTS

3.1 Debris flow mobility reconstructed without utilizing reduced friction coefficients

We reconstruct the relation between debris flow mobility and initial volume. In the experimental (Table S2) and numerical cases (Tables S3-S5), the volumes are based on distinct channel widths, in accordance with observed natural debris flows (Iverson, 1997). To eliminate potential discrepancy due to different channel widths, we define the non-dimensional initial volume $\hat{V}_0$ as $\hat{V}_0 = \bar{V}_0 / V_{ref}$, where $\bar{V}_0$ is the initial volume per unit width and V_{ref} is that of a reference case (i.e., Case EXP-F), i.e., $V_{ref} = 3$ m^2. Similarly, the non-dimensional run-out distance $\hat{L}$ is defined as $\hat{L} = L / L_{ref}$, where L_{ref} is the run-out distance in Case EXP-F. Figure 4 shows the dependence of debris flow mobility, characterized by efficiency e (Figure 4a) and run-out distance $\hat{L}$ (Figure 4b), on non-dimensional initial volume over a 31° sloping ramp. Figure S5 presents the corresponding results for a 40° sloping ramp. In agreement with observations (Iverson 1997; Lucas et al., 2014), the mobility computed using the two-phase flow model (Li et al., 2018a) described above increases progressively as initial volume increases. Obviously, a debris flow over a steep slope has higher mobility than its mild-slope counterpart when all other conditions remain the same (c.f. results Tables S3-S5). Bed erosion, water content, and grain-size heterogeneity also enhance debris flow mobility, echoing previous findings from field and experimental data (Iverson, 1997; Legros, 2002; Rickenmann, 2005). When the initial volume is sufficiently small, the efficiency remains constant because the debris flow would terminate on the sloping ramp before reaching the runout pad, and so $e = \cot\theta$ =1.664. Moreover, predictions from three typical empirical relationships (Corominas, 1996;

Rickmann, 1999; Lucas et al., 2014) are included for comparison, which are unable to resolve the effects of bed erosion, water content, and grain-size heterogeneity. It can be seen that the computed efficiency for fixed-bed debris flows agrees with the most recently derived empirical relationship, based on velocity-dependent friction weakening (Lucas et al., 2014) (Table S6). However, whilst Figure 4 and Figure S5 show a positive correlation between mobility (in terms of efficiency e and run-out distance $\hat{L}$) and initial volume, the data fail to collapse on a single curve. Arguably, this is because the correlation between mobility and initial volume is purely geometrical, and does not contain any information relating to debris flow dynamics (Staron & Lajeunesse, 2007). In light of these results, it is suggested that initial volume alone is inadequate to characterize debris flow mobility.

FIGURE 4. Dependence of debris flow mobility on initial volume over a 31° sloping ramp. (a) Debris flow efficiency e against non-dimensional initial volume $\hat{V}_0$. Solid, dotted and dashed lines respectively present empirical results for laboratory-scale, intermediate and large field-scale cases. (b) Non-dimensional debris flow run-out distance $\hat{L}$ against non-dimensional initial volume $\hat{V}_0$.

3.2 Debris flow energetics: Grain-energy release

We probe into the energetics of the USGS large-scale experimental debris flows (Iverson et al., 2011) by evaluating the evolution of energy components and energy changes per unit width for both fixed-bed Case EXP-F (Figure 5) and erodible bed Case EXP-E (Figure 6).

The energy is conserved from initiation to final stoppage, characterizing the energy balance, as illustrated by $\Delta E \approx \Delta E_s + \Delta E_f \approx 0$ (Figures 5b and 6b). For the fixed-bed

523 case, Figure 5a, the gravitational potential energy E_G of both the liquid and solid
524 phases decreases monotonically, being progressively transformed into kinetic energy
525 (E_K) and fluctuation energy (E_{TK}), and dissipated by bed resistance (E_R) and
526 fluctuation motions (E_D). For the erodible-bed case, Figure 6a shows that E_G initially
527 decreases, then increases due to bed erosion, peaks and subsequently decreases as
528 the debris flow peters out. Meanwhile, E_G and, where applicable, the potential
529 energy of the eroded material E_{Gb}, are gradually converted into kinetic energy (E_K)
530 and fluctuation energy (E_{TK}), and dissipated by bed resistance (E_R) and fluctuation
531 motions (E_D), similar to the fixed-bed case. Note that E_{TK} is negligible, even though
532 its effect on debris flow kinetics is discernible (Li et al., 2018a).

533 Most notably, we find that the grains as a whole release energy to the liquid phase at
534 debris flow stoppage. For the liquid phase, the energy change $\Delta E_f > 0$ at stoppage
535 (i.e., $t =$ 40 s), indicating that energy dissipated by bed resistance and fluctuation
536 motions ($E_{Rf} + E_{Df}$) exceeds the initial bulk energy (E_{T0f}) (Figure 5b, for the fixed-bed
537 case) and, where applicable, the potential energy of the eroded bed material (E_{Gbf})
538 (Figure 6b, for the erodible-bed case). For the solid phase, the reverse occurs as
539 $\Delta E_s < 0$. Moreover, the magnitudes of ΔE_s and ΔE_f are comparable with the peak
540 kinetic energy. Note that mass gain from bed erosion enhances energy transfer
541 because the grain-energy release of the erodible-bed case at stoppage (Figure 6b) is
542 considerably greater than its fixed-bed counterpart (Figure 5b).

543 Further, the energy change of the liquid phase ΔE_f is approximately equal to the
544 work done by solid-liquid interaction, E_{sf}, indicating that ΔE_f arises from
545 interaction with the solid phase. Concurrently, the energy change of the solid phase

546 ΔE_s is equal to the work done by liquid-solid interaction and interactions between
547 different-sized grains, i.e., $E_{fs} + E_{ss}$. Physically, the sum of interactive forces between
548 the liquid and solid grains and between different-sized grains must vanish according
549 to Newton's third law. However, the liquid and different-sized grains typically have
550 distinct velocities and so their interactive forces generate energy transfer. Noting that
551 previous studies reveal that water content and grain-size heterogeneity can enhance
552 debris flow mobility (Iverson, 1997; Legros, 2002; Rickenmann, 2005), the present
553 work suggests that it is the interactions between liquid and solid grains and between
554 different-sized grains that enable the effects of water content and grain-size
555 heterogeneity on debris flow mobility to be substantial.

556 Inter-phase energy transfer is a highly complex process. For the fixed-bed case
557 (Figure 5b), the transfer process involves three stages. First, ΔE_s increases and
558 ΔE_f decreases. Initially, the liquid moves freely and propagates faster downslope
559 than the solid grains; hence the solid-liquid interactive force $F_{sf} < 0$, and accordingly
560 $E_{sf} < 0$, leading to a decrease in ΔE_f. The growth in ΔE_s primarily arises from E_{fs},
561 which increases because the liquid-solid interactive force $F_{fs} > 0$ while E_{ss}
562 decreases with time. During the second stage, the energy changes of both phases
563 exhibit reverse behavior, i.e., ΔE_s decreases and ΔE_f increases. Due to energy
564 gain during the first stage, the solid grains gradually move faster than the liquid phase.
565 Consequently $F_{sf} > 0$ and the liquid phase absorbs energy from the solid phase;
566 meanwhile ΔE_s reduces mainly due to inter-phase and inter-grain size interactions.
567 Finally, when the debris flow gradually comes to rest, causing deposition on the
568 runout pad, both ΔE_f and ΔE_s become steady. Comparatively, in the erodible-bed

569 case (Figure 6b), at the early stage, $t < 0.6$ s, when the debris flow reaches the
570 erodible bed but erosion has not yet commenced, the debris flow exhibits similar
571 inter-phase energy transfer features to those observed during the first two stages of
572 the fixed-bed debris flow (Figure 5b), i.e., ΔE_s increases initially and then decreases,
573 whereas ΔE_f undergoes the opposite behaviour. Subsequently, a new cycle of
574 three-stage inter-phase energy transfer, similar to that in fixed-bed debris flow, is
575 triggered by rapid bed erosion and proceeds until the debris flow comes to a halt.

576

577
578 **FIGURE 5** Evolution of energy components and energy changes of USGS
579 experimental fixed-bed debris flows Case EXP-F (Iverson et al., 2011). (a) Evolution
580 of energy components, including kinetic energy (E_K), fluctuation kinetic energy (E_{TK}),
581 gravitational potential energy (E_G), and energy dissipation due to bed resistance (E_R)
582 and fluctuation motions (E_D) with the subscripts f and s denoting the liquid and
583 solid phases, respectively. (b) Evolution of energy changes of the solid-liquid mixture
584 (ΔE), solid phase (ΔE_s), and liquid phase (ΔE_f), and the work done by inter-phase
585 (E_{fs} and E_{sf}) and inter-grain size interaction forces (E_{ss}).

586

587

588 **FIGURE 6** Evolution of energy components and energy changes of USGS
589 experimental erodible-bed debris flows Case EXP-E (Iverson et al., 2011). (a)
590 Evolution of energy components, including kinetic energy (E_K), fluctuation kinetic
591 energy (E_{TK}), gravitational potential energy (E_G), potential energy due to sediment
592 exchange with the bed (E_{Gb}), and energy dissipation due to bed resistance (E_R) and
593 fluctuation motions (E_D) with the subscripts f and s denoting the liquid and solid
594 phases, respectively. (b) Evolution of energy changes of the solid-liquid mixture (ΔE),
595 solid phase (ΔE_s), and liquid phase (ΔE_f), and the work done by inter-phase (E_{fs}

596 and E_{sf}) and inter-grain size interaction forces (E_{ss}).

597

598 The role of grains in debris flow energetics is size-dependent (Figures 7 and 8).
599 During the initial stage, the liquid phase releases energy to grains of all sizes as E_{fsk}
600 increases; and fine grains release energy to coarse grains as E_{ssk} decreases for fine
601 grains (Figures 7a-b and Figures 8a-b) and increases for coarse grains (Figures 7c-d
602 and Figures 8c-d). Besides, $E_{fsk}+E_{ssk}$ of fine grains decreases, whereas that of
603 coarse grains increases, indicating that fine grains release energy while coarse grains
604 absorb energy. Physically, this process lubricates the grains, especially coarse grains,
605 and facilitates the initiation and acceleration of debris flow, as evidenced by an
606 increase in kinetic energy (Figure 5b and Figure 6b). Subsequently, reverse energy
607 transfer is exhibited as the grains release energy to the liquid, and coarse grains
608 transfer energy to fine grains, sustaining the debris flow until it stops, during which
609 time the bulk kinetic energy decreases (Figure 5b and Figure 6b). Specifically, E_{fsk} of
610 all grains and E_{ssk} of coarse grains decrease (Figures 7c-d and Figures 8c-d), while
611 E_{ssk} of fine grains increases (Figures 7a-b and Figures 8a-b). Also, $E_{fsk}+E_{ssk}$ of fine
612 grains increases, while that of coarse grains decreases. Note that the mass gain from
613 bed erosion enhances such processes because the magnitudes of E_{fsk}, E_{ssk} and
614 $E_{fsk}+E_{ssk}$ in the erodible-bed case (Figure 8) are generally larger than their
615 counterparts in the fixed-bed case (Figure 7). Until final stoppage, coarse grains
616 release energy over both fixed and erodible beds because $E_{fsk}+E_{ssk} < 0$ (Figures 7c-d
617 and Figures 8c-d), whereas fine grains in the erodible-bed case release energy
618 because $E_{fsk}+E_{ssk} < 0$, as shown in Figures 8a-b, contrary to fine grains absorbing
619 energy in the fixed-bed case (see Figures 7a-b).

FIGURE 7 Evolution of energy changes in size-specific grains for fixed-bed Case EXP-F. (a-b) fine grains; (c-d) coarse grains. E_{fsk} and E_{sfk} represent work done by the inter-phase interaction force, and E_{ssk} represents work done by the inter-grain size interaction force.

FIGURE 8 Evolution of energy changes in size-specific grains for erodible-bed Case EXP-E. (a-b) fine grains; (c-d) coarse grains. E_{fsk} and E_{sfk} represent work done by the inter-phase interaction force, and E_{ssk} represents work done by the inter-grain size interaction force.

3.3 Grain-energy release as a function of initial volume

We now evaluate the grain-energy release for all the numerical cases (Table S3-S5). The non-dimensional grain-energy release is defined as $\Delta\hat{E}_s = abs(\Delta E_s)/abs(E_{ref})$, where E_{ref} is the grain-energy release in Case EXP-F. The dependence of non-dimensional grain-energy release $\Delta\hat{E}_s$ on initial volume is illustrated for the two ramps in Figure 9 and Figure S6. Similar to debris flow mobility (Figure 4 and Figure S5), grain-energy release increases with initial debris flow volume and ramp length, and is enhanced by mass gain from bed erosion, water content, and grain-size heterogeneity. Furthermore, the steeper ramp usually leads to elevated grain-energy release (comparing Figure 9 to Figure S6).

FIGURE 9 Dependence of non-dimensional grain-energy release $\Delta\hat{E}_s$ on non-dimensional initial debris flow volume $\hat{V}_0$ over a 31° sloping ramp.

3.4 Debris flow mobility correlated with grain-energy release

We now delve into the relationship between debris flow mobility and grain-energy release at final stoppage. Interestingly, the mobility of debris flow correlates closely with grain-energy release in terms of both efficiency e (Figure 10a) and run-out distance $\hat{L}$ (Figure 10b).

As shown in Figure 10a, when the initial volume is very small, the efficiency is determined solely by slope angle, i.e., $e = \cot\theta$. For intermediate initial volumes, the efficiency is jointly determined by initial volume and ramp length; therefore, it follows different relations with non-dimensional grain-energy release, depending on ramp length, but independent of mass gain from bed erosion, water content, grain-size heterogeneity, and ramp slope angle. If the initial volume is sufficiently large, its effect on efficiency reigns over the ramp, rendering a collapse of the data from both laboratory- and field-scale cases onto a single curve. Therefore, the non-dimensional grain-energy release, which incorporates the effects of initial volume and topography, is more suitable than initial volume alone for characterizing the mobility of debris flow. This proposition is further reinforced by the universal relation between run-out distance and grain energy release ($\hat{L} \sim \Delta\hat{E}_s$) shown in Figure 10b, regardless of ramp length, slope angle, initial volume, water content, bed erosion, and grain-size heterogeneity.

Given the above observations, we propose that grain-energy release governs debris flow mobility, therefore facilitating a bridge between debris flow mobility and internal

energy transfer. It is well recognized that experimental observation of grain-energy release of debris flow is much more challenging than that of the initial volume. This is perhaps why debris flow energetics have rarely, if ever, been related to debris flow mobility. Therefore, this topic invites future investigation as driven from the present findings. Indeed, it is quite common that computational science leads to new theories and inspires new experiments, or suggests important variables to be investigated in laboratory tests.

FIGURE 10 Debris flow mobility versus grain-energy release. (a) Dependence of efficiency e on non-dimensional grain-energy release $\Delta\hat{E}_s$; (b) Dependence of non-dimensional run-out distance $\hat{L}$ on non-dimensional grain-energy release $\Delta\hat{E}_s$.

4 DISCUSSION

4.1 Inter-phase energy transfer

The results in Section 3.2 lead us to propose an energy transfer pattern between liquid, fine grains, and coarse grains in debris flow (Figure 11). During the initial stage of a mass-release debris flow, the liquid phase transfers energy to the grains, and fine grains release energy to coarse grains. Later, the grains release energy to the liquid, and coarse grains release energy to fine grains, thus sustaining the debris flow until final stoppage. Up to final stoppage, the coarse grains release energy ($E_{fsk}+E_{ssk}<0$), whilst the fine grains either absorb ($E_{fsk}+E_{ssk}>0$) or release ($E_{fsk}+E_{ssk}<0$) energy, depending on bed erosion (Figures 7 and 8); and concurrently, among those grains releasing energy, the larger the grain size, the higher the grain energy release, and this grain-size dependence can be modified by initial volume, water content,

grain-size heterogeneity, and bed erosion (Figure S7). The energy transfer pattern appears to underpin previous experimental findings (Iverson, 1997; Johnson et al., 2012; de Haas et al., 2015; Kaitna et al., 2016) that interactions between fine and coarse grains can increase debris flow mobility.

FIGURE 11 Energy transfer between liquid, fine grains, and coarse grains in debris flow.

4.2 Implications

Our finding that grain-energy release governs high mobility of debris flow provides insight into the fundamental mechanisms of debris flows due to solid-liquid mass release. In particular, initial volume, as a univariate variable, is inadequate for characterizing debris flow mobility. The grain-energy release appears to be more suitable. Furthermore, a friction-reduction mechanism (e.g., Legros, 2002; Iverson et al., 2011; Lube et al., 2012; Pudasaini & Miller, 2013; Lucas et al., 2014) is not a prerequisite for the high mobility of debris flows. By contrast, inter-phase and inter-grain size interactions play primary roles and so should be explicitly incorporated in debris flow models. This implies that existing quasi single-phase models (e.g., Takahashi et al., 1992; Iverson, 1997; McDougall & Hungr, 2005; Medina et al., 2008; Armanini, 2009; Rosatti & Begnudelli, 2013; Iverson & George, 2014; Lucas et al., 2014; Frank et al., 2015; Cuomo et al., 2016; Xia et al., 2018; Federico & Cesali, 2019; Gregoretti et al., 2019), two-phase models that presume a single grain size (e.g.,

718 Pitman & Le, 2005; Pelanti et al., 2008; Pailha & Pouliquen, 2009; Pudasaini, 2012;
719 Kowalski & McElwaine, 2013; Bouchut et al., 2015), and energy balance-based
720 models (Wang et al., 2010; Bouchut et al., 2015) may need to be enhanced for more
721 accurate resolution of debris flows. Likewise, additional large-scale debris flow
722 experiments using flumes with varied bed topography and observations of natural
723 debris flows over irregular and steep slopes are needed in order to support further
724 model development. Indeed, the present modelling results inevitably bear some
725 degree of uncertainty because empirical closures for inter-grain size interaction, liquid
726 and solid fluctuations, and mass exchange with the bed have tentatively been used.
727 Therefore, this topic invites more systematic fundamental investigation. As multiple
728 physics are involved in the present model, scaling analysis is required to evaluate
729 their relative importance in resolving the mechanisms underlying the high mobility of
730 debris flows due to solid-liquid mass release.

731 The first of its kind, the present work has implications in future assessments of debris
732 flow hazards and in informing mitigation and adaptation strategies. This is significant
733 and particularly timely, noting the acceleration in glacier melt and increasing trend in
734 extreme precipitation amount, intensity, and frequency (Donat et al., 2013), which are
735 likely to trigger more debris flows. The study also has broad implications for
736 unravelling a spectrum of earth surface processes including heavily sediment-laden
737 floods due to storms and glacier lake outbursts (Laronne & Reid, 1993; Xiao, Young,
738 & Prévost, 2010; Grinsted, Hvidberg, Campos, Dahl-Jensen, 2017; Cook, Andermann,
739 Gimbert, Adhikari, & Hovius, 2018; Hook, 2019), and subaqueous debris flows and

740 turbidity currents in rivers, reservoirs, estuaries, and the ocean (Weirich, 1988; Wright
741 & Friedrichs, 2006; Talling et al., 2007; Armanini, 2013; Cao, Li, Pender, & Liu, 2015b;
742 Paull et al., 2018; Stevenson et al., 2018; Li, Cao, & Liu, 2019).
743

5 CONCLUSIONS

A recently developed depth-averaged two-phase flow model has been used to investigate debris flow mobility, without evoking reduced friction coefficients. Debris flow mobility computed by the model increases with initial volume and is enhanced by mass gain from bed erosion, water content, and grain-size heterogeneity, echoing previous experimental and field studies. It is found that whilst the energy balance holds and fine and coarse grains play distinct roles in debris flow energetics, the grains as a whole release energy to the liquid due to inter-phase and inter-grain size interactions, and the grain-energy release correlates closely with debris flow mobility. This leads us to propose that the mobility of debris flow due to solid-liquid mass release is governed by grain-energy release, thereby facilitating a bridge between debris flow mobility and internal energy transfer.

Grain-energy release appears to be more suitable than initial volume to characterize debris flow mobility. Also, grain-energy release characterizes the interactions between liquid and solid grains and between different-sized grains, which play primary roles in debris flow dynamics. In light of the present finding from physically-based numerical modelling, the quest for a friction-reduction mechanism may not be viable, which concurs with Iverson (2016) who comments that there is insufficient experimental evidence to support the friction-reduction hypotheses. Meanwhile, it is implied that single-phase flow models, two-phase flow models that

presume a single grain size, and energy balance-based models may need to be enhanced for resolving debris flows and hence assessment of such hazards.

Although the closure models are far from perfect, the findings obtained from the present model are qualitatively encouraging and physically meaningful. Indeed, all models for earth surface flows inevitably contain uncertainty arising from empirical closure, which invites systematic fundamental investigation in the future. Further experiments are needed to enhance the understanding of debris flows and to further validate the present findings. Moreover, as multiple physics are involved in the present model, scaling analysis is required to evaluate their relative importance in debris flow dynamics. Extension to two dimensions would be useful for practical applications to natural debris flows.

ACKNOWLEDGEMENTS

This study was supported by Natural Science Foundation of China under Grants NO. 11672212 and 11432015.

DATA AVAILABILITY STATEMENT

The data that support the findings of this study are available from the corresponding author upon reasonable request.

784 **NOTATION**

B_i	width of the i-th control volume (m)
C_k	depth-averaged size-specific volumetric sediment concentration (-)
C_f	depth-averaged volume fraction of the liquid phase (-)
d_{50}	particle size at which 50% of the sediments are finer (m)
e	debris flow efficiency (-)
E_D	energy dissipation due to fluctuation motions (J)
E_{fs}	work done by inter-phase interaction force for the solid phase (J)
E_G	gravitational potential energy of debris flow (J)
E_{Gb}	potential energy due to sediment exchange with the bed (J)
E_{Gs}, E_{Gf}	gravitational potential energy of the solid and liquid phases in debris flow (J)
E_k	kinetic energy of debris flow (J)
E_{ks}, E_{kf}	kinetic energy of the solid and liquid phases in debris flow (J)
E_R	energy dissipation due to bed resistance (J)
E_{sf}	work done by inter-phase interaction force for the liquid phase (J)
E_{ss}	work done by inter-grain size interaction force (J)
E_{T0}	initial energy of debris flow (J)
E_{TK}	fluctuation kinetic energy of debris flow (J)
E_{TKs}, E_{TKf}	fluctuation kinetic energy of the solid and liquid phases debris flow (J)
F_{fs_k}	size-specific depth-averaged interphase interaction force for the solid phase (kg m^{-1} s^{-2})
F_{s_kf}	size-specific depth-averaged interphase interaction force for the liquid phase (kg m^{-1} s^{-2})
F_{s-s_k}	size-specific depth-averaged inter-grain size interaction drag force (kg m^{-1} s^{-2})

f , s , m	subscript denoting the liquid phase, solid phase, mixture (-)
g	gravitational acceleration (ms^{-2})
H_i	vertical distance between the mass center of debris flow of the i-th control volume and the datum level (m)
H_{bi}	vertical distance between the mass center of the $i-$th control volume for bed deformation and the datum level (m)
h	debris flow depth (m)
h_b	bed deformation depth (m)
i	index denoting the control volume (-)
k	subscript denoting the k-th sediment size
L	run-out distance of debris flow (m)
L_{ref}	run-out distance of debris flow of a refence case (m)
$\hat{L}$	non-dimensional run-out distance of debris flow
p	porosity of bed sediments (-)
TK_{sk}	size-specific depth-averaged fluctuation kinetic energy of the solid phase ($m^2\ s^{-3}$)
TK_f	depth-averaged fluctuation kinetic energy of the liquid phase ($m^2\ s^{-3}$)
t	time (s)
U_f	depth-averaged velocity of the liquid phase in the x-direction ($m\ s^{-1}$)
U_{sk}	size-specific depth-averaged velocity of the solid phase in the x-direction ($m\ s^{-1}$)
$\bar{V}_0$	initial volume per unit width (m^2)
$\hat{V}_0$	non-dimensional initial volume
V_b	volume of bed sediments (m^3)
$\bar{V}_{ref}$	initial volume per unit width of a reference case
x	streamwise coordinate (m)
x_d	distance from the mass release point along the channel to the point where the flow reaches the horizontal reference datum (m)

z_b	bed elevation (m)
ΔE_f	energy change of the liquid phase in debris flow (J)
ΔE_s	energy change of the solid phase in debris flow (J)
$\Delta \hat{E}_s$	non-dimensional grain-energy release (-)
ΔE_{sk}	energy change of size-specific grains (J)
Δt	time step (s)
Δx	spatial step (m)
ε_f	depth-averaged dissipation rate of liquid fluctuation kinetic energy (m^2 s^{-3})
ε_{sk}	Size-specific depth-averaged dissipation rate of solid fluctuation kinetic energy (m^2 s^{-3})
θ	angle of bed slope (-)
θ_f	water content of bed sediments (-)
σ	standard deviation of sediment composition (-)
ρ_f , ρ_s	densities of the liquid and solid phases (kg m^{-3})
$\tau_{s_k b}$, τ_{fb}	bed shear stresses for the solid and liquid phases respectively (kg m^{-1} s^{-2})

785

786

787

REFERENCES

Armanini, A. (2013). Granular flows driven by gravity. *Journal of Hydraulic Research*, *51*(2), 111-120. doi: 10.1080/00221686.2013.788080

Armanini, A., Fraccarollo, L., & Rosatti, G. (2009). Two-dimensional simulation of debris flows in erodible channels. *Computers & Geosciences*, *35*(5), 993-1006. doi: 10.1016/j.cageo.2007.11.008

Bouchut, F., Fernandez-Nieto, E. D., Mangeney, A., & Narbona-Reina, G. (2015). A two-phase shallow debris flow model with energy balance. *ESAIM: Mathematical Modelling and Numerical Analysis*, *49*(1), 101-140. doi: 10.1051/m2an/2014026

Cao, Z., Hu, P., Hu, K., Pender, G., & Liu, Q. (2015a). Modelling roll waves with shallow water equations and turbulent closure. *Journal of Hydraulic Research*, *53*(2), 161-177 (2015). doi: 10.1080/00221686.2014.950350.

Cao, Z., Li, J., Pender, G., & Liu, Q. (2015b). Whole-process modeling of reservoir turbidity currents by a double layer-averaged model. *Journal of Hydraulic Engineering*, *141*(2), 04014069. doi: 10.1061/(ASCE)HY.1943-7900.0000951.

Chen, M., Liu, X., Wang, X., Zao, T., & Zhou, J. (2019). Contribution of Excessive Supply of Solid Material to a Runoff-Generated Debris Flow during Its Routing Along a Gully and Its Impact on the Downstream Village with Blockage Effects. *Water*, *11*(1), 169. doi:10.3390/w11010169

Cook, K. L., Andermann, C., Gimbert, F., Adhikari, B. R., & Hovius, N. (2018). Glacial lake outburst floods as drivers of fluvial erosion in the Himalaya. *Science*, *362*(6410), 53-57. doi: 10.1126/science.aat4981.

Corominas, J. (1996). The angle of reach as a mobility index for small and large landslides. *Canadian Geotechnical Journal*, *33*(2), 260-271. doi: 10.1139/t96-005.

Cuomo, S., Pastor, M., Capobianco, V., & Cascini, L. (2016). Modelling the space-time bed entrainment for flow-like landslide. *Engineering Geology*, *212*, 10-20. doi: 10.10116/j.enggeo.2016.07.011.

de Haas, T., Braat, L., Leuven, J. R., Lokhorst, I. R., & Kleinhans, M. G. (2015). Effects of debris flow composition on runout, depositional mechanisms, and deposit morphology in laboratory experiments. *Journal of Geophysical Research: Earth Surface*, *120*(9), 1949-1972. doi: 10.1002/2015JF003525.

Donat, M. G., Alexander, L. V., Yang, H., Durre, I., Vose, R., Dunn, R. J. H., ... & Hewitson, B. (2013). Updated analyses of temperature and precipitation extreme indices since the beginning of the twentieth century: The HadEX2 dataset. *Journal of Geophysical Research: Atmospheres*, *118*(5), 2098-2118. doi: 10.1002/jgrd.50150

Federico, F., & Cesali, C. (2019). Effects of granular collisions on the rapid coarse-grained materials flow. *Gèotechnique Letters*, *9*(4), 1-6. doi: 10.1680/jgele.18.00223.

Frank, F., McArdell, B.W., Huggel, C., & Vieli, A. (2015). The importance of entrainment and bulking on debris flow runout modeling: examples from the Swiss Alps. *Natural Hazards and Earth System Sciences*, *15*(11), 2569-2583. doi:10.5194/nhess-15-2569-2015.

Gidaspow, D. (1994). *Multiphase Flow and Fluidization: Continuum and Kinetic Theory Descriptions*. Cambridge, MA: Academic Press.

834 Goren, L., & Aharonov, E. (2007). Long runout landslides: the role of frictional heating
835 and hydraulic diffusivity. *Geophysical Research Letters*, *34*(7), 248-265. doi:
836 10.1029/2006GL02889
837 Gray, J. M. N. T., & Chugunov, V. A. (2006). Particle-size segregation and diffusive
838 remixing in shallow granular avalanches. *Journal of Fluid Mechanics*, *569*,
839 365-398. doi: 10.1017/S0022112006002977.
840 Gregoretti, C., Degetto, M., Bernard, M., & Boreggio, M. (2018). The debris flow
841 occurred at Ru Secco Creek, Venetian Dolomites, on 4 August 2015: analysis of
842 the phenomenon, its characteristics and reproduction by models. *Frontier in*
843 *Earth Sciences*, *6*, 80. doi: 10.3389/feart.2018.00080.
844 Gregoretti, C., Stancanelli, L., Bernard, M., Degetto, M., Boreggio, M., & Lanzoni, S.
845 (2019). Relevance of erosion processes when modelling in-channel gravel debris
846 flows for efficient hazard assessment. *Journal of Hydrology*, *568*, 575-591;
847 doi10.1016/j.jhydrol.2018.10.001
848 Grinsted, A., Hvidberg, C. S., Campos, N., & Dahl-Jensen, D. (2017). Periodic
849 outburst floods from an ice-dammed lake in East Greenland. *Scientific reports*,
850 *7*(1), 9966. doi: 10.1038/s41598-017-07960-9
851 Hayashi, J. N., & Self, S. (1992). A comparison of pyroclastic flow and debris
852 avalanche mobility. *Journal of Geophysical Research: Solid Earth*, *97*(B6),
853 9063-9071. doi: 10.1029/92JB00173
854 Hirano, M. (1971). River bed degradation with armouring. *Transactions of Japanese*
855 *Society of Civil Engineering*, *195*(11), 55-65 (in Japanese).
856 Hook, J. M. (2019). Extreme sediment fluxes in a dryland flash flood. *Scientific*
857 *Reports*, *9*, 1686. doi: 10.1038/s41598-019-38537-3
858 Hungr, O., & Evans, S. G. (2004). Entrainment of debris in rock avalanches: an

analysis of a long run-out mechanism. *Geological Society of America Bulletin*, *116*(9-10), 1240-1252. doi: 10.1130/B25362.1.

Hürlimann, M., Abanco, C., Moya, J., & Vilajosana, I. (2014). Results and experiences gathered at the Rebaixader debris-flow monitoring site, Central Pyrenees, Spain. *Landslides*, *11*(6), 161–175. https://doi.org/10.1007/s10346-013-0452-y.

Iverson, R. M. (1997). The physics of debris flows. *Reviews of geophysics*, *35*(3), 245-296. doi: 10.1029/97RG00426.

Iverson, R. M. (2012). Elementary theory of bed-sediment entrainment by debris flows and avalanches. *Journal of Geophysical Research: Earth Surface*, *117*, F03006, doi:10.1029/2011JF002189.

Iverson, R. M. (2016). Comment on “The reduction of friction in long-runout landslides as an emergent phenomenon” by Brandon C. Johnson et al. *Journal of Geophysical Research: Earth Surface*, *121*(11), 2238-2242. doi: 10.1002/2016JF003979.

Iverson, R. M., & George, D. L. (2014). A depth-averaged debris-flow model that includes the effects of evolving dilatancy. I. Physical basis. *Proceedings of the Royal Society A: Mathematical, Physical and Engineering Sciences*, *470*(2170), 20130819. doi: 10.1098/rspa.2013.0819.

Iverson, R. M., George, D. L., Allstadt, K., Reid, M. E., Collins, B. D., Vallance, J. W., ... & Baum, R. L. (2015). Landslide mobility and hazards: implications of the 2014 Oso disaster. *Earth and Planetary Science Letters*, *412*, 197-208. doi: 10.1016/j.epsl.2014.12.020.

Iverson, R. M., Logan, M., LaHusen, R. G., & Berti, M. (2010). The perfect debris flow?

882 Aggregated results from 28 large-scale experiments. *Journal of Geophysical*
883 *Research: Earth Surface*, *115*(F3). doi: 10.1029/2009JF001514.
884 Iverson, R. M., Reid, M. E., Logan, M., LaHusen, R. G., Godt, J. W., & Griswold, J. P.
885 (2011). Positive feedback and momentum growth during debris-flow entrainment
886 of wet bed sediment. *Nature Geoscience*, *4*(2), 116-121. doi: 10.1038/ngeo1040
887 Jenkins, J. T., & Richman, M. W. (1985). Grad's 13 moment system for a dense gas of
888 inelastic spheres. *Archive for Rational Mechanics and Analysis*, *87*, 355-377.
889 Johnson, B. C., Campbell, C. S., & Melosh, H. J. (2016). The reduction of friction in
890 long runout landslides as an emergent phenomenon. *Journal of Geophysical*
891 *Research: Earth Surface*, *121*(5), 881-889. doi: 10.1002/2015JF003751.
892 Johnson, C. G., Kokelaar, B. P., Iverson, R. M., Logan, M., LaHusen, R. G., & Gray, J.
893 M. N. T. (2012). Grain-size segregation and levee formation in geophysical mass
894 flows. *Journal of Geophysical Research: Earth Surface*, *117*(F01032). doi:
895 10.1029/2011JF002185.
896 Kaitna, R., Palucis, M. C., Yohannes, B., Hill, K. M., & Dietrich, W. E. (2016). Effects
897 of coarse grain size distribution and fine particle content on pore fluid pressure
898 and shear behavior in experimental debris flows. *Journal of Geophysical*
899 *Research: Earth Surface*,*121*(2), 415-441. doi: 10.1002/2015JF003725.
900 Kowalski, J., & McElwaine, J. N. (2013). Shallow two-component gravity-driven flows
901 with vertical variation. *Journal of Fluid Mechanics*, *714*, 434-462. doi:
902 10.1017/jfm.2012.489.
903 Kean, J. W., McCoy, S. W., Tucker, G. E., Staley, D. M., & Coe, J. A. (2013).
904 Runoff-generated debris flows: Observations and modeling of surge initiation,
905 magnitude, and frequency. *Journal of Geophysical Research: Earth Surface*, *118*,
906 2190–2207. doi:10.1002/jgrf.20148, 2013

907 Laronne, J. B., & Reid, I. (1993). Very high rates of bedload sediment transport by
908 ephemeral desert rivers. *Nature*, *366*, 148-150. doi: 10.1038/366148a0.
909 Lanzoni, S., Gregoretti, C., & Stancanelli, L. (2017). Coarse-grained debris flow
910 dynamics on erodible beds. *Journal of Geophysical Research: Earth Surface*,
911 *122*, 592-614, doi: 0.1002/2016JF004046.
912 Legros, F. (2002). The mobility of long-runout landslides. *Engineering Geology*, *63*(3),
913 301-331. doi: 10.1016/S0013-7952(01)00090-4.
914 Li, J., Cao, Z., & Liu, Q. (2019). Waves and sediment transport due to granular
915 landslides impacting reservoirs. *Water Resources Research*, *55*(1), 495-518. doi:
916 10.1029/2018WR023191
917 Li, J., Cao, Z., Hu, K., Pender, G., & Liu, Q. (2018a). A depth-averaged two-phase
918 model for debris flows over erodible bed. *Earth Surface Processes and*
919 *Landforms*, *43*(4), 817-839. doi: 10.1002/esp.4283.
920 Li, J., Cao, Z., Hu, K., Pender, G., & Liu, Q. (2018b). A depth-averaged two-phase
921 model for debris flows over fixed beds. *International Journal of Sediment*
922 *Research*, *33*(4), 462-477. doi: 10.1016/j.ijsrc.2017.06.003.
923 Linares-Guerrero, E., Goujon, C., & Zenit, R. (2007). Increased mobility of bidisperse
924 granular avalanches. *Journal of Fluid Mechanics*, *593*, 475-504. doi:
925 10.1017/S0022112007008932.
926 Lube, G., Cronin, S. J., Manville, V., Procter, J. N., Cole, S. E., & Freundt, A. (2012).
927 Energy growth in laharic mass flows. *Geology*, *40*(5), 475-478. doi:
928 10.1130/G32818.1.
929 Lucas, A., Mangeney, A., & Ampuero, J. P. (2014). Frictional velocity-weakening in
930 landslides on Earth and on other planetary bodies. *Nature Communications, 5*(3),

3417. doi: 10.1038/ncomms4417.

Ma, C., Deng, J., & Wang, R. (2018). Analysis of the triggering conditions and erosion of a runoff triggered debris flow in Miyun County, Beijing, China. *Landslide*, *15*(12), 2475-2485. doi: 10.1007/s10346-018-1080-3.

Mangeney, A., Tsimring, L. S., Volfson, D., Aranson, I. S., & Bouchut, F. (2007). Avalanche mobility induced by the presence of an erodible bed and associated entrainment. *Geophysical Research Letters*, *34*, L22401. doi: 10.1029/2007GL031348.

Medina, V., Hürlimann, M., & Bateman, A. (2008). Application of FLATModel, a 2D finite volume code, to debris flows in the northeastern part of the Iberian Peninsula. *Landslides*, *5*(1), 127-142. doi: 10.1007/s10346-007-0102-3.

McDougall, S., & Hungr, O. (2005). Dynamic modelling of entrainment in rapid landslides. *Canadian Geotechnical Journal*, *42*(5): 1437–1448. doi: 10.1139/t05-064

Pailha, M., & Pouliquen, O. (2009). A two-phase flow description of the initiation of underwater granular avalanches. *Journal of Fluid Mechanics*, *633*, 115–135. doi: 10.1017/S0022112009007460.

Paull, C. K., Talling, P. J., Maier, K. L., Parsons, D., Xu, J., Caress, D. W., ... & Chaffey, M. (2018). Powerful turbidity currents driven by dense basal layers. *Nature Communications*, *9*(1), 4114. doi: 10.1038/s41467-018-06254-6.

Pelanti, M., Bouchut, F., & Mangeney, A. (2008). A Roe-Type scheme for twophase shallow granular flows over variable topography. *ESAIM: Mathematical Modelling and Numerical Analysis*, *42*, 851–885. doi: 10.1051/m2an:2008029

Perinotto, H., Schneider, J. L., Bachèlery, P., Le Bourdonnec, F. X., Famin, V., &

955 Michon, L. (2015). The extreme mobility of debris avalanches: A new model of
956 transport mechanism. *Journal of Geophysical Research: Solid Earth*, *120*(12),
957 8110-8119. doi: 10.1002/2015JB011994.
958 Pirulli, M., & Pastor M. (2012). Numerical study on the entrainment of bed material
959 into rapid landslides. *Géotechnique*, *62*(11), 959-972. doi:
960 10.1680/geot.10.P.074.
961 Pitman, E. B., Nichita, C. C., Patra, A. K., Bauer, A. C., Bursik, M., & Weber, A. (2003).
962 A model of granular flows over an erodible surface. *Discrete and Continuous*
963 *Dynamical Systems Series B*, *3*(4), 589-600. doi: 10.3934/dcdsb.2003.3.589.
964 Pitman, E. B., & Le, L. (2005). A two-fluid model for avalanche and debris flows.
965 *Proceedings of the Royal Society of London A: Mathematical, Physical and*
966 *Engineering Sciences*, *363*, 1573–1602. doi: 10.1098/rsta.2005.1596
967 Pudasaini, S. P. (2012). A general two-phase debris flow model. *Journal of*
968 *Geophysical Research: Earth Surface*, *117*, F03010. doi:
969 10.1029/2011JF002186.
970 Pudasaini, S. P., & Miller, S. A. (2013). The hypermobility of huge landslides and
971 avalanches. *Engineering Geology, 157*, 124-132. doi:
972 10.1016/j.enggeo.2013.01.012.
973 Rickenmann, D. (1999). Empirical relationships for debris flows. *Natural hazards*,
974 *19*(1), 47-77. doi: 10.1023/A:100806422.
975 Rickenmann, D. (2005). Runout prediction methods. In M. Jakob, & O. Hungr (Eds.),
976 *Debris-Flow Hazards and Related Phenomena* (pp. 305-324). Berlin, Heidelberg:
977 Springer
978 Rodi, W. (1993). *Turbulence models and their application in hydraulics*. Boca Raton,
979 Florida: CRC Press.

Rosatti, G., & Begnudelli, L. (2013). Two-dimensional simulation of debris flows over erodible bed: enhancing the TRENT2D model by using a well-balanced generalized Roe-type solver. *Computers and Fluids*, *71*, 179–195. doi: 10.1016/j.compfluid.2012.10. 006.

Staron, L., & Lajeunesse, E. (2009). Understanding how volume affects the mobility of dry debris flows. *Geophysical Research Letters*, *36*(12), L12402. doi:10.1029/2009GL038229.

Shreve, R. L. (1968). Leakage and fluidization in air-layer lubricated avalanches. *Geological Society of America Bulletin*, *79*(5), 653-658. doi: 10.1130/0016-7606(1968)79[653:LAFIAL]2.0.CO;2.

Singer, K. N., McKinnon, W. B., Schenk, P. M., & Moore, J. M. (2012). Massive ice avalanches on Iapetus mobilized by friction reduction during flash heating. *Nature Geoscience*, *5*(8), 574-578. doi: 10.1038/ngeo1526.

Stevenson, C. J., Feldens, P., Georgiopoulou, A., Schönke, M., Krastel, S., Piper, D. J., ... & Mosher, D. (2018). Reconstructing the sediment concentration of a giant submarine gravity flow. *Nature Communications*, *9*(1), 2616. doi: 10.1038/s41467-018-05042-6.

Talling, P. J., Wynn, R. B., Masson, D. G., Frenz, M., Cronin, B. T., Schiebel, R., ... & Georgiopoulou, A. (2007). Onset of submarine debris flow deposition far from original giant landslide. *Nature*, *450*(7169), 541-544. doi: 10.1038/nature06313.

Takahashi, T., Nakagawa, H., Harada, T., & Yamashiki, Y. (1992). Routing debris flows with particle segregation. *Journal of Hydraulic Engineering*, *118*(11), 1490–1507. doi: 10.1061/(ASCE)0733-9429(1992)118:11(1490)

1003 Utili, S., Zhao, T., & Houlsby, G. T. (2015). 3D DEM investigation of granular column
1004 collapse: evaluation of debris motion and its destructive power. *Engineering*
1005 *Geology*, *186*, 3-16. doi: 10.1016/j.enggeo.2014.08.018
1006 Vallance, J. W., & Scott, K. M. (1997). The Osceola Mudflow from Mount Rainier:
1007 Sedimentology and hazard implications of a huge clay-rich debris flow.
1008 *Geological Society of America Bulletin, 109*(2), 143-163. doi:
1009 10.1130/0016-7606(1997)109<0143:TOMFMR>2.3.CO;2.
1010 Wang, X., Morgenstern, N. R., & Chan, D. H. (2010). A model for geotechnical
1011 analysis of flow slides and debris flows. *Canadian Geotechnical Journal*, *47*(12),
1012 1401-1414. doi: 10.1139/T10-039.
1013 Wang, Y. F., Dong, J. J., & Cheng, Q. G. (2017). Velocity-dependent frictional
1014 weakening of large rock avalanche basal facies: Implications for rock avalanche
1015 hypermobility? *Journal of Geophysical Research: Solid Earth*, *122*(3), 1648-1676.
1016 doi: 10.1002/2016JB013624
1017 Weirich, H. H. (1988). Field evidence for hydraulic jumps in subaqueous sediment
1018 gravity flows. *Nature*, *332*, 626-629. doi: 10.1038/332626a0
1019 Wright, L. D., & Friedrichs, C. T. (2006). Gravity-driven sediment transport on
1020 continental shelves: a status report. *Continental Shelf Research*, *26*(17-18),
1021 2092-2107. doi: 10.1016/j.csr.2006.07.008.
1022 Wu, W. (2007). *Computational river dynamics*. London: Taylor & Francis.
1023 Xia, C.C., Li, J., Cao, Z., Liu, Q., & Hu, K. (2018). A quasi single-phase model for
1024 debris flows and its comparison with a two-phase model. *Journal of Mountain*

Science, *15*(5), 1071-1089. doi: 10.1007/s11629-018-4886-5

Xiao, H., Young, Y. L., & Prévost, J. H. (2010). Hydro-and morpho-dynamic modeling of breaking solitary waves over a fine sand beach. Part II: Numerical simulation. *Marine Geology*, *269*(3-4), 119-131. doi: 10.1016/j.margeo.2009.12.008.

List of figure captions

FIGURE 1 Flume geometry for USGS debris flow experiments [from Iverson et al. (2011)].

FIGURE 2 Flume geometry used in (a) laboratory-scale numerical case studies (adapted from Iverson et al., 2011); (b) field-scale numerical case studies. The topography has an upstream ramp of uniform inclination angle θ, length L_0 and height H_0, followed by a horizontal runout pad at the downstream end.

FIGURE 3 Sketch of control volume used for energy calculation. H_i is vertical distance between the mass center of debris flow of the i-th control volume and the datum level, and is accordingly defined by Eq. (3).

FIGURE 4. Dependence of debris flow mobility on initial volume over a 31° sloping ramp. (a) Debris flow efficiency e against non-dimensional initial volume $\hat{V}_0$. Solid, dotted and dashed lines respectively present the empirical results for laboratory-scale, intermediate and large field-scale cases. (b) Non-dimensional debris flow run-out distance $\hat{L}$ against non-dimensional initial volume $\hat{V}_0$.

FIGURE 5 Evolution of energy components and energy changes of USGS experimental fixed-bed debris flows Case EXP-F (Iverson et al., 2011). (a) Evolution of energy components, including kinetic energy (E_K), fluctuation kinetic energy (E_{TK}), gravitational potential energy (E_G), and energy dissipation due to bed resistance (E_R) and fluctuation motions (E_D) with the subscripts f and s denoting the liquid and solid phases, respectively. (b) Evolution of energy changes of the solid-liquid mixture (ΔE), solid phase (ΔE_s), and liquid phase (ΔE_f), and the work done by inter-phase (E_{fs} and E_{sf}) and inter-grain size interaction forces (E_{ss}).

FIGURE 6 Evolution of energy components and energy changes of USGS experimental erodible-bed debris flows Case EXP-E (Iverson et al., 2011). (a) Evolution of energy components, including kinetic energy (E_K), fluctuation kinetic

energy (E_{TK}), gravitational potential energy (E_G), potential energy due to sediment exchange with the bed (E_{Gb}), and energy dissipation due to bed resistance (E_R) and fluctuation motions (E_D) with the subscripts f and s denoting the liquid and solid phases, respectively. (b) Evolution of energy changes of the solid-liquid mixture (ΔE), solid phase (ΔE_s), and liquid phase (ΔE_f), and the work done by inter-phase (E_{fs} and E_{sf}) and inter-grain size interaction forces (E_{ss}).

FIGURE 7 Evolution of energy changes in size-specific grains for fixed-bed Case EXP-F. (a-b) fine grains; (c-d) coarse grains. E_{fsk} and E_{sfk} represent work done by the inter-phase interaction force, and E_{ssk} represents work done by the inter-grain size interaction force.

FIGURE 8 Evolution of energy changes in size-specific grains for erodible-bed Case EXP-E. (a-b) fine grains; (c-d) coarse grains. E_{fsk} and E_{sfk} represent work done by the inter-phase interaction force, and E_{ssk} represents work done by the inter-grain size interaction force.

FIGURE 9 Dependence of non-dimensional grain-energy release $\Delta\hat{E}_s$ on non-dimensional initial debris flow volume $\hat{V}_0$ over a 31° sloping ramp.

FIGURE 10 Debris flow mobility versus grain-energy release. (a) Dependence of efficiency e on non-dimensional grain-energy release $\Delta\hat{E}_s$; (b) Dependence of non-dimensional run-out distance $\hat{L}$ on non-dimensional grain-energy release $\Delta\hat{E}_s$.

FIGURE 11 Energy transfer between liquid, fine grains, and coarse grains in debris flow.

FIGURES

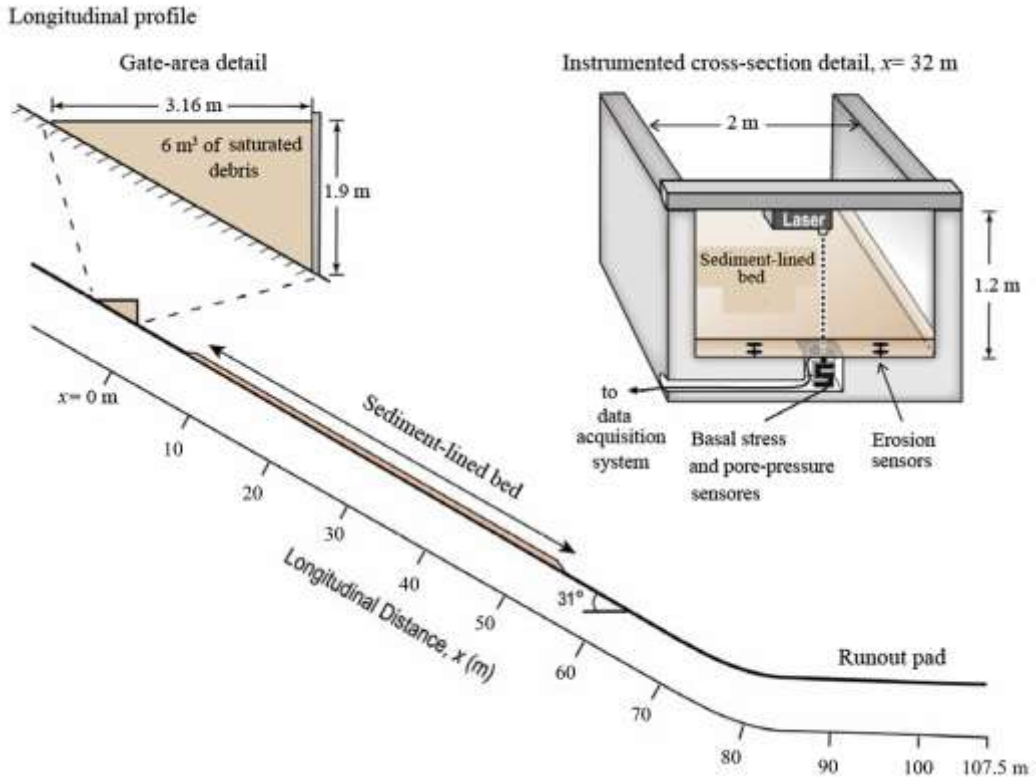

FIGURE 1 Flume geometry for USGS debris flow experiments [from Iverson et al. (2011)].

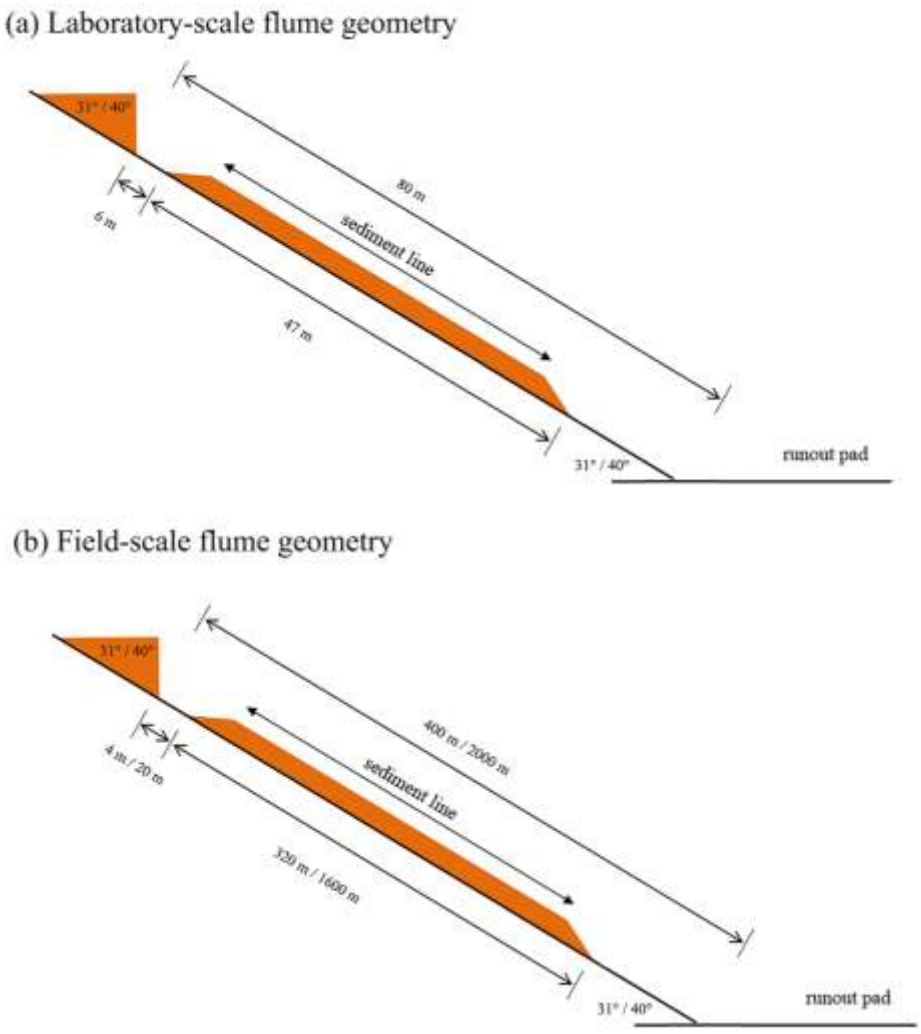

FIGURE 2 Flume geometry used in (a) laboratory-scale numerical case studies (adapted from Iverson et al., 2011); (b) field-scale numerical case studies. The topography has an upstream ramp of uniform inclination angle θ, length L_0 and height H_0, followed by a horizontal runout pad at the downstream end.

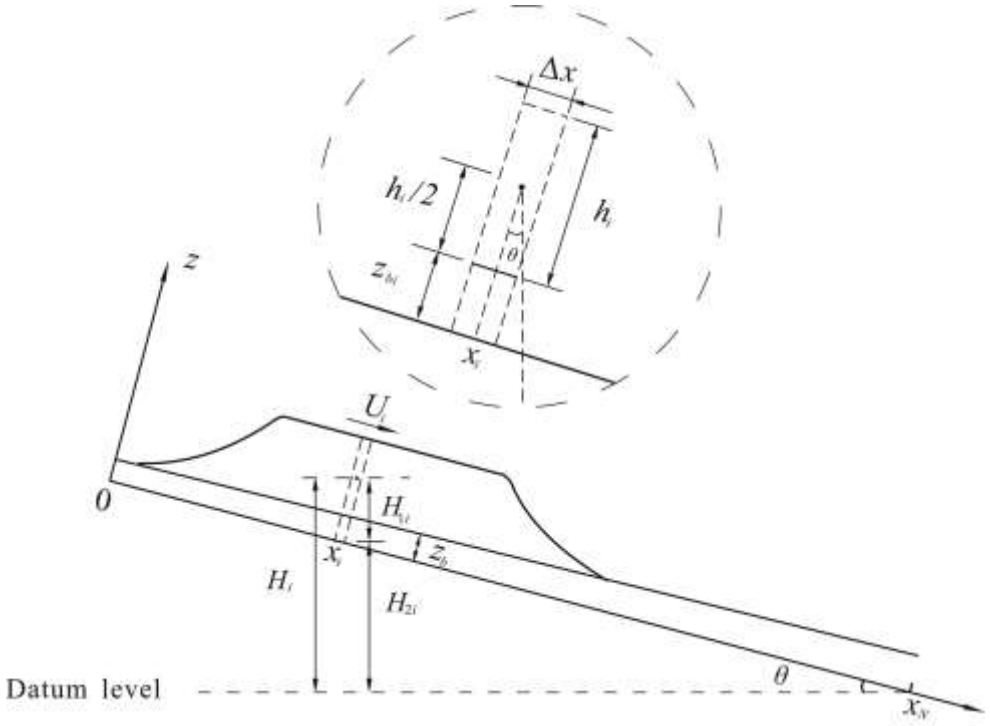

FIGURE 3 Sketch of control volume used for energy calculation. H_i is vertical distance between the mass center of debris flow of the i-th control volume and the datum level, and is accordingly defined by Eq. (2).

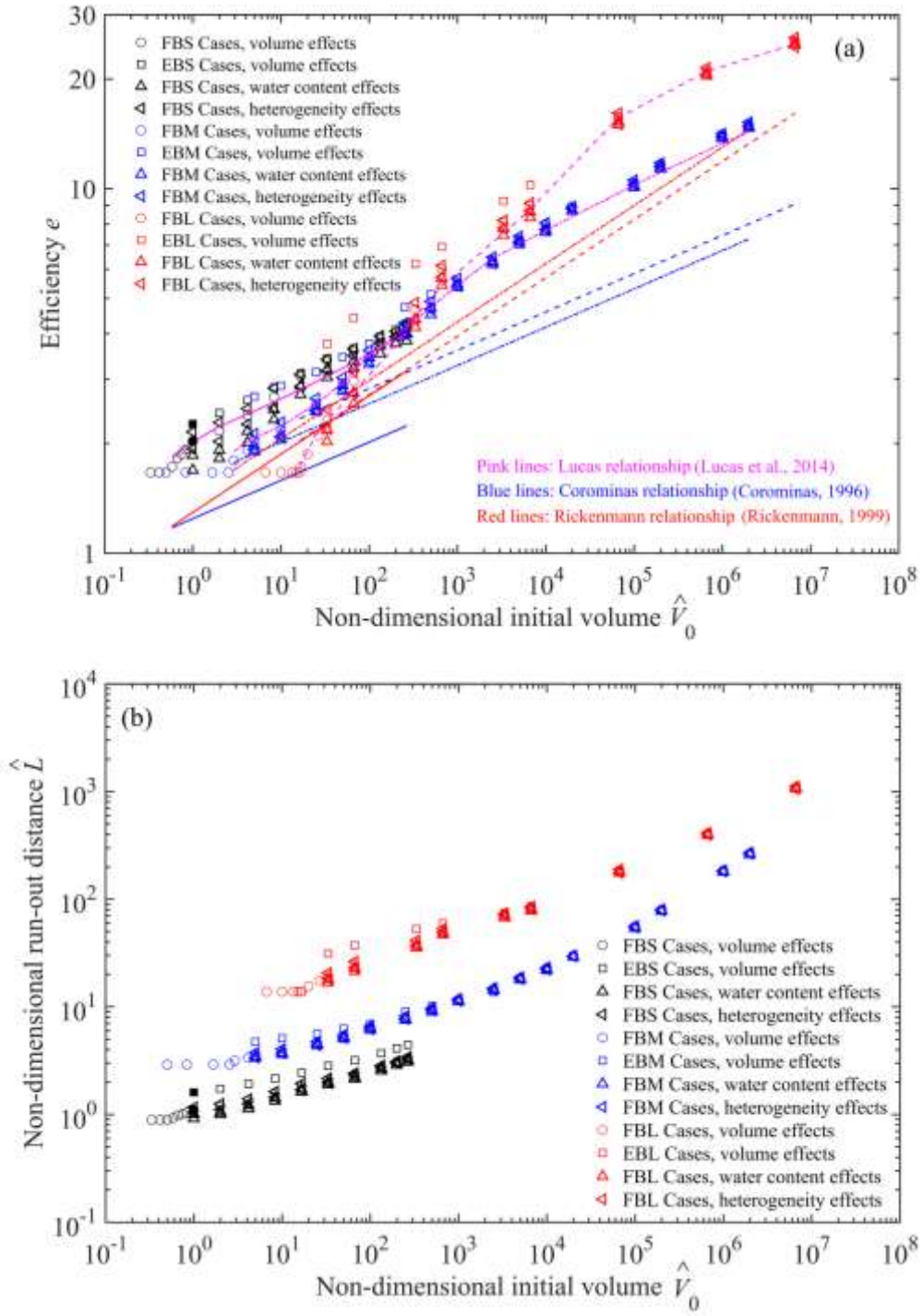

FIGURE 4. Dependence of debris flow mobility on initial volume over a 31° sloping ramp. (a) Debris flow efficiency e against non-dimensional initial volume $\hat{V}_0$. Solid, dotted and dashed lines respectively denote empirical results for laboratory-scale, intermediate and large field-scale cases. (b) Non-dimensional debris flow run-out distance $\hat{L}$ against non-dimensional initial volume $\hat{V}_0$.

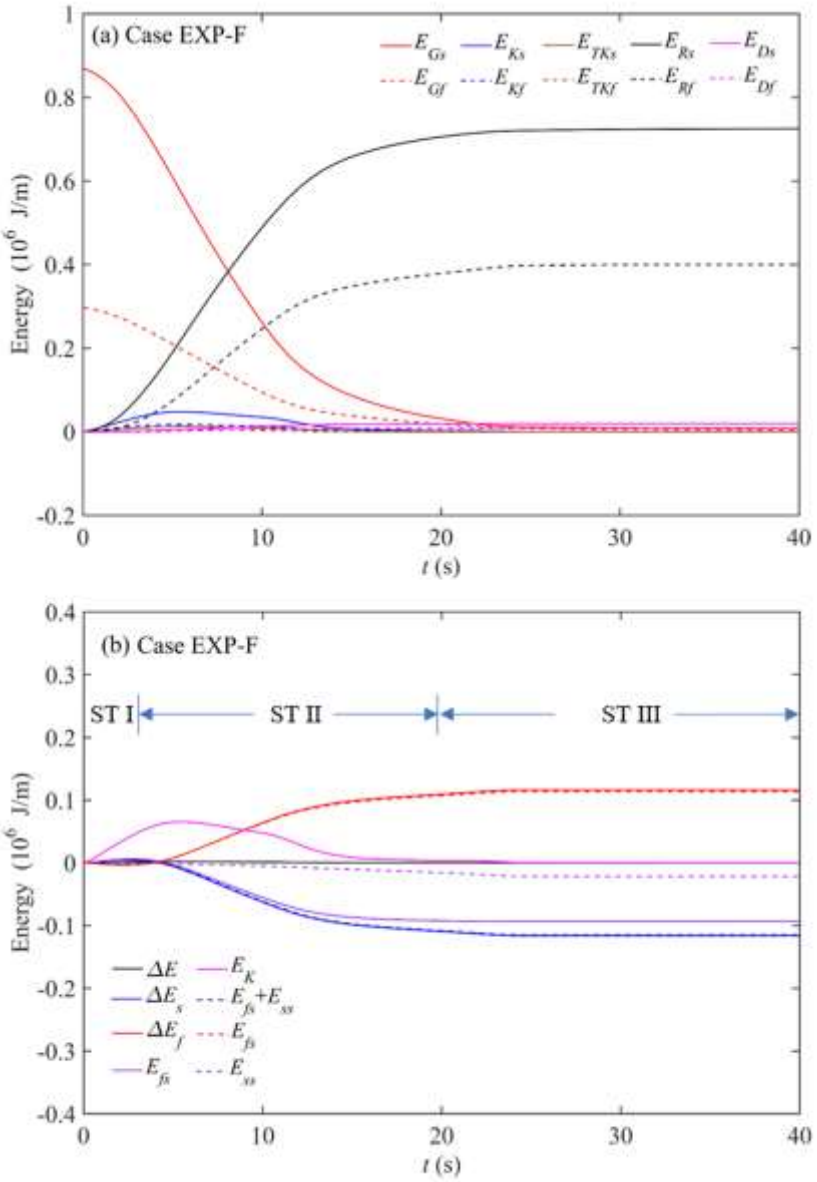

FIGURE 5 Evolution of energy components and energy changes of USGS experimental fixed-bed debris flows Case EXP-F (Iverson et al., 2011). (a) Evolution of energy components, including kinetic energy (E_K), fluctuation kinetic energy (E_{TK}), gravitational potential energy (E_G), and energy dissipation due to bed resistance (E_R) and fluctuation motions (E_D) with the subscripts f and s denoting the liquid and solid phases, respectively. (b) Evolution of energy changes of the solid-liquid mixture (ΔE), solid phase (ΔE_s), and liquid phase (ΔE_f), and the work done by inter-phase (E_{fs} and E_{sf}) and inter-grain size interaction forces (E_{ss}).

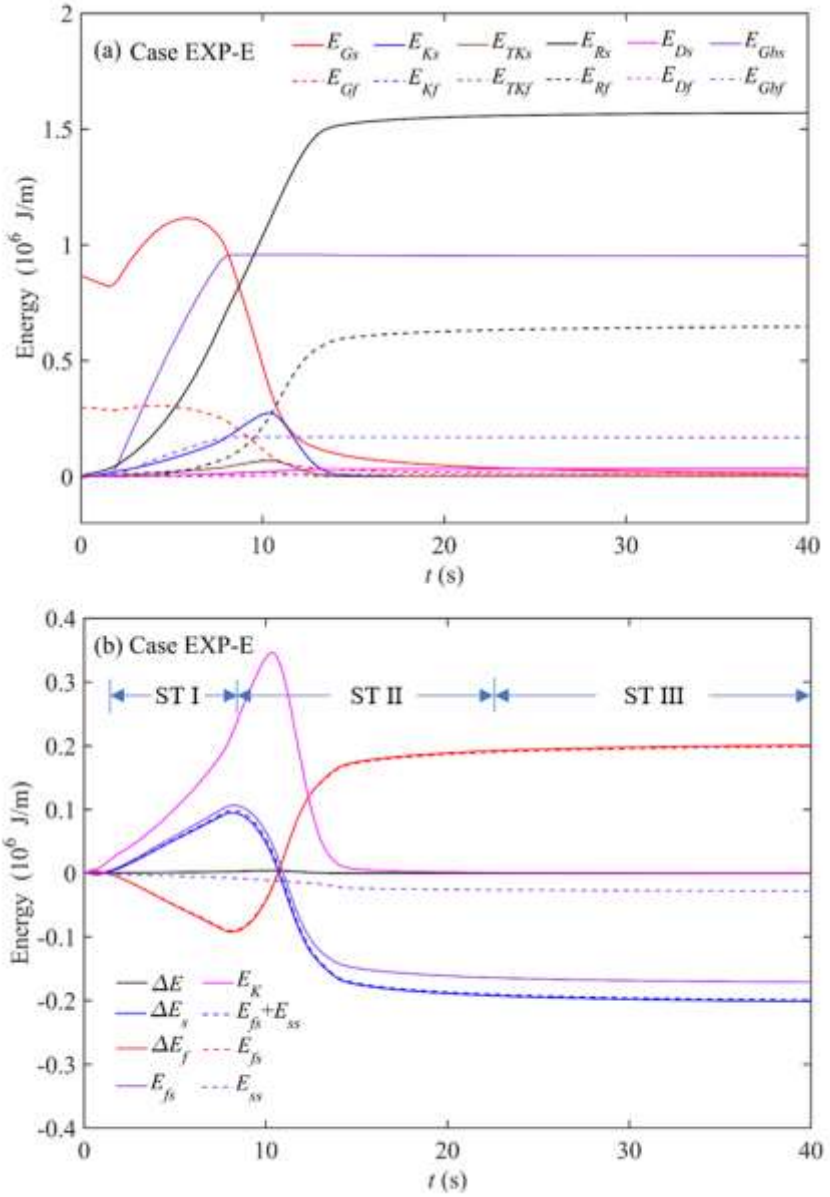

FIGURE 6 Evolution of energy components and energy changes of USGS experimental erodible-bed debris flows Case EXP-E (Iverson et al., 2011). (a) Evolution of energy components, including kinetic energy (E_K), fluctuation kinetic energy (E_{TK}), gravitational potential energy (E_G), potential energy due to sediment exchange with the bed (E_{Gb}), and energy dissipation due to bed resistance (E_R) and fluctuation motions (E_D) with the subscripts f and s denoting the liquid and solid phases, respectively. (b) Evolution of energy changes of the solid-liquid mixture (ΔE), solid phase (ΔE_s), and liquid phase (ΔE_f), and the work done by inter-phase (E_{fs} and E_{sf}) and inter-grain size interaction forces (E_{ss}).

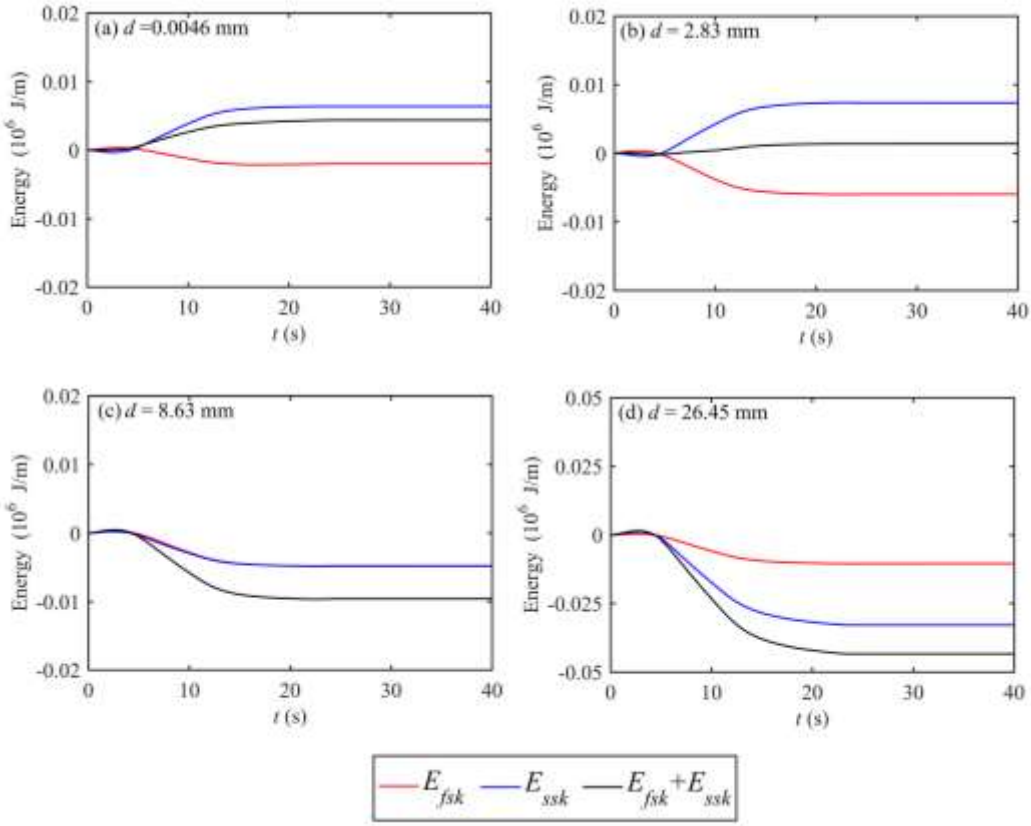

FIGURE 7 Evolution of energy changes in size-specific grains for fixed-bed Case EXP-F. (a-b) fine grains; (c-d) coarse grains. E_{fsk} and E_{sfk} represent work done by the inter-phase interaction force, and E_{ssk} represents work done by the inter-grain size interaction force.

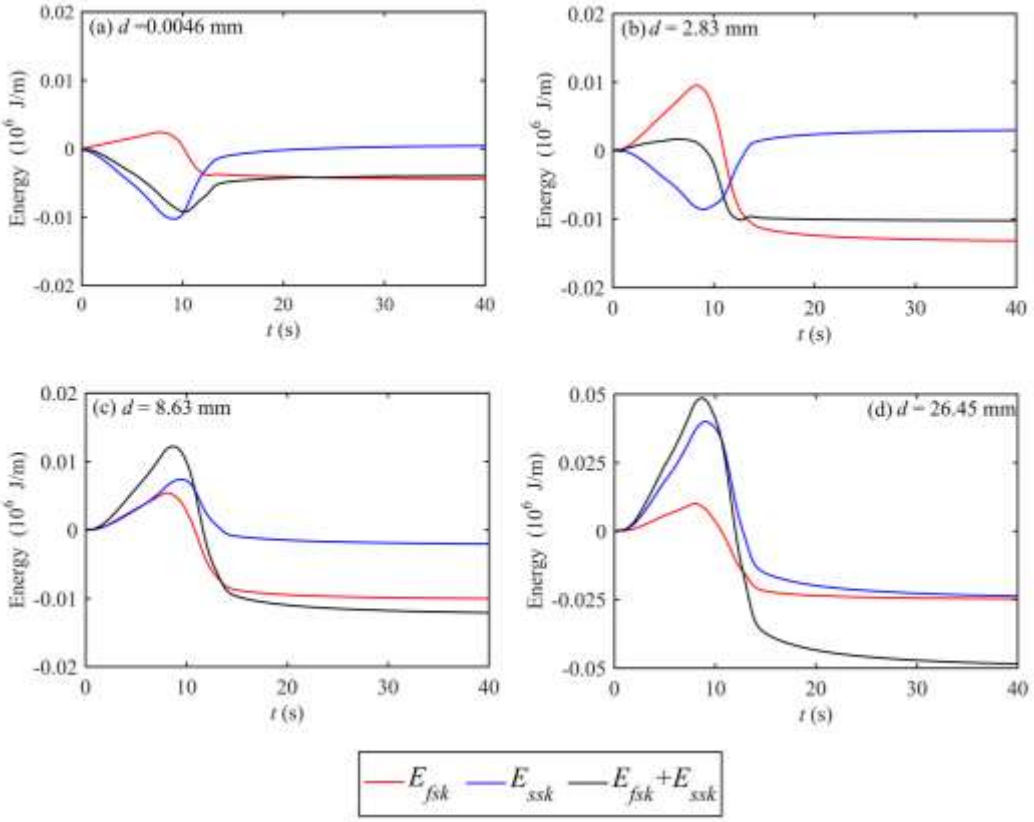

FIGURE 8 Evolution of energy changes in size-specific grains for erodible-bed Case EXP-E. (a-b) fine grains; (c-d) coarse grains. E_{fsk} and E_{sfk} represent work done by the inter-phase interaction force, and E_{ssk} represents work done by the inter-grain size interaction force.

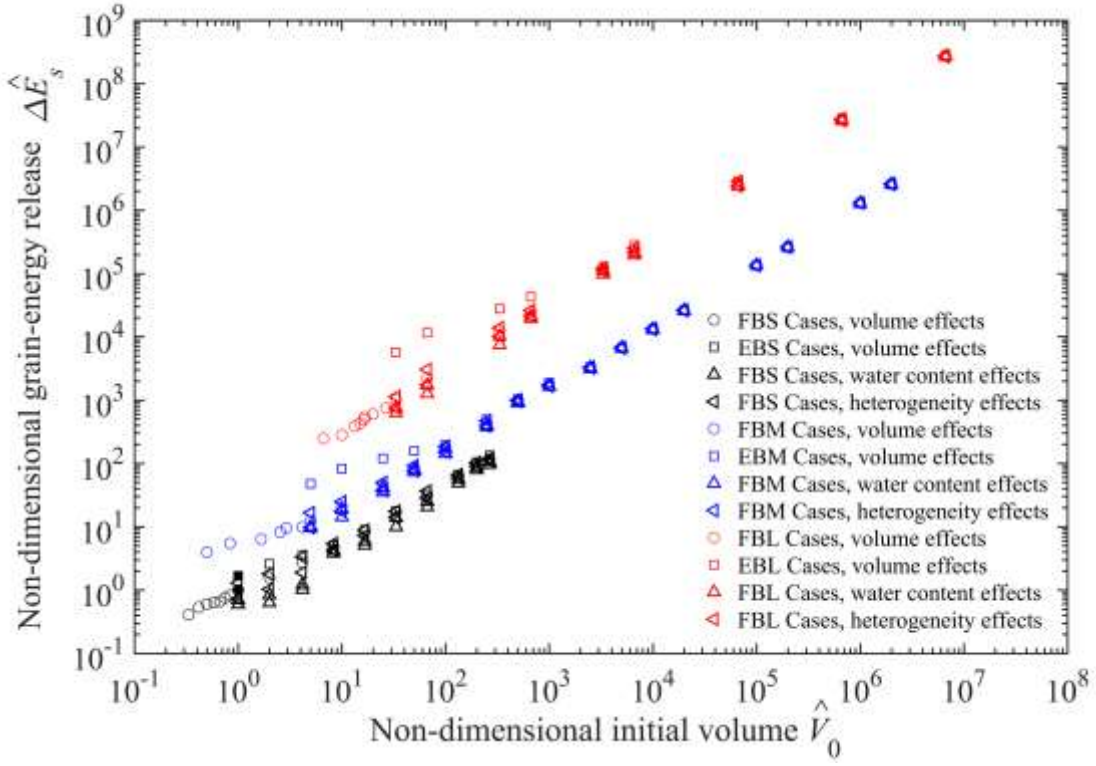

FIGURE 9 Dependence of non-dimensional grain-energy release $\Delta\hat{E}_s$ on non-dimensional initial debris flow volume $\hat{V}_0$ over a 31° sloping ramp.

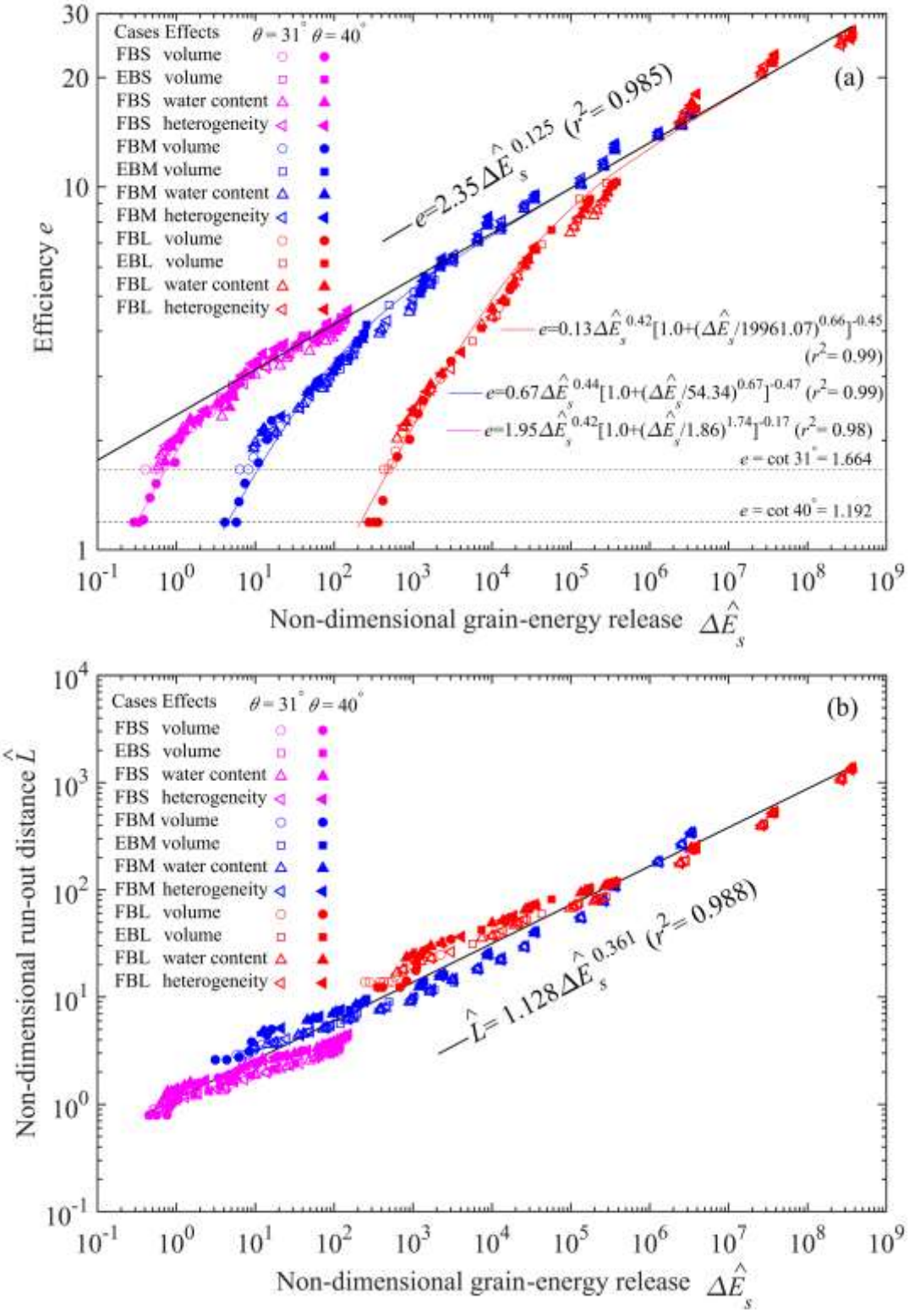

FIGURE 10 Debris flow mobility versus grain-energy release. (a) Dependence of efficiency e on non-dimensional grain-energy release $\Delta\hat{E}_s$; (b) Dependence of non-dimensional run-out distance $\hat{L}$ on non-dimensional grain-energy release $\Delta\hat{E}_s$.

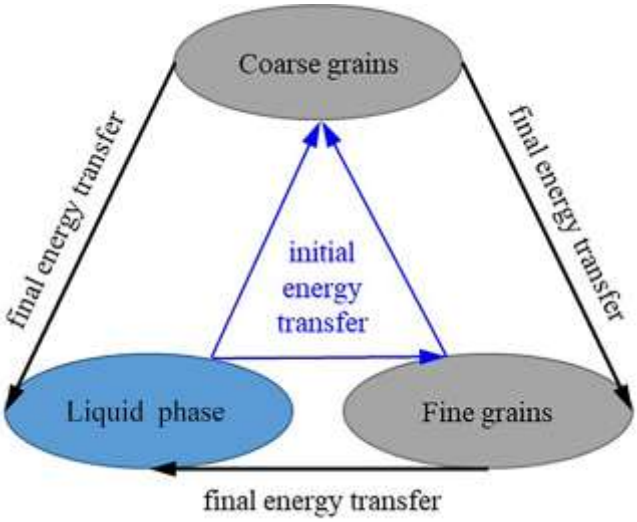

FIGURE 11 Energy transfer between liquid, fine grains, and coarse grains in debris flow.